



## Smart antioxidant function enhancing (SAFE) nucleic acid therapy for ROS-related chronic diseases and comorbidities

Zhiguo Lu<sup>a,b,e,1</sup>, Ruichen Zhao<sup>a,b,e,1</sup>, Yi Li<sup>d,1</sup>, Jianze Wang<sup>a</sup>, Jing Guo<sup>a,e</sup>, Chaobo Bai<sup>c</sup>,  
Jing Chen<sup>c</sup>, Jun Yang<sup>a,b,e</sup>, Yiwan Geng<sup>a,b,e</sup>, Tianlu Zhang<sup>a,e</sup>, Yanyue Wu<sup>a,b,e</sup>, Xiyue Jiao<sup>a,e</sup>,  
Yining Wang<sup>d,\*\*</sup>, Junliang Yuan<sup>c,\*\*\*</sup>, Xin Zhang<sup>a,b,e,\*</sup>

<sup>a</sup> State Key Laboratory of Biochemical Engineering, Institute of Process Engineering, Chinese Academy of Sciences, Beijing, 100190, PR China

<sup>b</sup> School of Chemical Engineering, University of Chinese Academy of Sciences, Beijing, 100049, PR China

<sup>c</sup> Department of Neurology, Peking University Sixth Hospital, Peking University Institute of Mental Health, Beijing, 100191, PR China

<sup>d</sup> Department of Radiology, State Key Laboratory of Complex Severe and Rare Diseases, Peking Union Medical College Hospital, Chinese Academy of Medical Sciences and Peking Union Medical College, Beijing, 100730, PR China

<sup>e</sup> Key Laboratory of Biopharmaceutical Preparation and Delivery, Institute of Process Engineering, Chinese Academy of Sciences, Beijing, 100190, PR China

### ARTICLE INFO

#### Keywords:

Smart antioxidant function enhancing (SAFE) strategy  
Reactive oxygen species  
Nucleic acid drugs  
Keap1-Nrf2-ARE pathway  
ROS-Associated chronic diseases and comorbidities

### ABSTRACT

Reactive oxygen species (ROS)-mediated oxidative stress exacerbates chronic diseases such as organ damage and neurodegenerative disorders. The Keap1-Nrf2-ARE pathway is a widely distributed endogenous antioxidant system. However, ROS under redox homeostasis regulates a wide range of life activities. Therefore, smart scavenging of excess ROS under pathological conditions is essential to treat chronic diseases safely. This study reports a smart antioxidant function enhancement (SAFE) strategy. On-demand release of nucleic acid drugs in a pathological ROS environment smartly activates the endogenous antioxidant system, thereby smartly alleviating oxidative stress in an exogenous antioxidant-independent manner. Through structural modulation and ligand modification, we develop SAFE nanoparticles based on nanohybrid complexes (SAFE-complex) adapted to brain delivery of nucleic acid drugs. SAFE-complex with homogeneous monodisperse structure efficiently treat ROS-related neurodegenerative diseases while protecting the major organ from oxidative stress damage. Moreover, SAFE-complex can stabilize storage in the form of freeze-dried powder. These data indicate that SAFE nanoparticles hold promise for treating ROS-related chronic diseases and comorbidities through rational transformation.

### 1. Introduction

Oxidative stress caused by excess reactive oxygen species (ROS) [1–3] can exacerbate chronic diseases, such as neurodegenerative diseases [4,5] and organ injuries [6–9], by mediating cell death through mitochondrial dysfunction. Especially for Parkinson, its pathogenesis is closely related to ROS accumulation and oxidative stress. (1) Mitochondrial dysfunction will lead to excessive ROS production. These ROS will damage mitochondrial DNA, proteins and lipids, form a vicious

cycle, further destroy mitochondrial function, lead to more ROS production, and ultimately lead to neuronal apoptosis. (2) Excessive ROS can also lead to the occurrence of inflammatory response, which will further affect the function and survival of cells and the generation and accumulation of chronic damage to organs. Long-term pharmacological treatment of chronic diseases further raises the risk of organ injuries. Therefore, the downregulation of ROS is expected to affect the treatment of ROS-related chronic disease comorbidities positively. Exogenous antioxidants can rapidly scavenge ROS but have short potency and are

Peer review under responsibility of KeAi Communications Co., Ltd.

\* Corresponding author. State Key Laboratory of Biochemical Engineering, Institute of Process Engineering, Chinese Academy of Sciences, Beijing, 100190, PR China.

\*\* Corresponding author.

\*\*\* Corresponding author.

E-mail addresses: [wangyining@pumch.cn](mailto:wangyining@pumch.cn) (Y. Wang), [junliangyuan@bjmu.edu.cn](mailto:junliangyuan@bjmu.edu.cn) (J. Yuan), [xzhang@ipe.ac.cn](mailto:xzhang@ipe.ac.cn) (X. Zhang).

<sup>1</sup> Zhiguo Lu, Ruichen Zhao and Yi Li have contributed equally to this work.

<https://doi.org/10.1016/j.bioactmat.2023.09.004>

Received 28 June 2023; Received in revised form 5 September 2023; Accepted 8 September 2023

2452-199X/© 2023 The Authors. Publishing services by Elsevier B.V. on behalf of KeAi Communications Co. Ltd. This is an open access article under the CC BY-NC-ND license (<http://creativecommons.org/licenses/by-nc-nd/4.0/>).

unsuitable for treating chronic diseases. In contrast, the Keap1-Nrf2-ARE pathway is an overall endogenous antioxidant system *in vivo*. Therefore, activation of the Keap1-Nrf2-ARE pathway is expected to achieve a long-lasting downregulation of ROS independent of exogenous antioxidants [10,11].

Nuclear factor E2-related factor 2 (Nrf2) is a crucial transcription factor for intracellular redox homeostasis and can activate endogenous antioxidant action by binding to the antioxidant response element (ARE) [12,13]. Kelch-like ECH-associated protein 1 (Keap1), a negative regulator of Nrf2, mediates the ubiquitination and degradation of Nrf2 to keep Nrf2 underactive *in vivo* [14,15]. However, ROS under redox homeostasis involves multiple life activities *in vivo*, such as providing and transmitting energy, promoting cellular metabolism, and initiating and regulating various metabolic and signaling pathways [14,16–19]. Therefore, smart scavenging of excess ROS under pathological conditions is the key to targeting ROS for the treatment of chronic diseases.

Common drugs that target ROS are antioxidants such as epigallocatechin gallate, quercetin, and nano-enzymes. However, these therapies are antioxidant-dependent and require long-term and high-frequency administration. In addition, these drugs remove pathological ROS while indiscriminately downregulate ROS in normal tissues, thereby increasing the safety risk. The small nucleic acid drug, such as small interfering RNA (siRNA), can degrade the mRNA of almost all therapeutic targets with high specificity through base complementary pairing, achieving long-lasting and highly specific inhibition of therapeutic targets [20,21]. Thus, siRNA is ideal for ROS clearance by targeting Keap1. Herein, we report a strategy termed Smart Antioxidant Function Enhancing (SAFE) for safely treating ROS-associated chronic diseases and their comorbidities through the smart release of siKeap1 in the pathological ROS microenvironment. We constructed SAFE nanoparticles based on nanohybrid complexes (SAFE-complex) suitable for delivery to the brain by a one-step synthesis method for Parkinson's disease (PD) and chronic liver injury (CLI) comorbidity (PD&CLI).

With the coordination of the cationic drug-carrying polymer dopamine-poly(phenylboronic acid-2-(dimethylamino) ethyl acrylate) (DP-P(B-DMAEA)), the focal target polymer dopamine-polyethylene glycol-RVG peptide (DP-PEG-RVG) and superparamagnetic iron oxide nanoparticles (SPIONs) by catechol in the polymers and Fe<sub>3</sub>O<sub>4</sub> in SPIONs, the organic polymers were tightly anchored on the inorganic nanoparticles to form a stable carrier and high density of positive charge for the firm loading and stable delivery of siKeap1 *in vivo* (Scheme 1a). Under redox homeostasis, DP-P(B-DMAEA) was not degraded. Instead, pathologically high levels of ROS mediated the conversion of the DP-P(B-DMAEA) cationic block to the anionic block, resulting in the release of siKeap1 (Schemes 1a and 1b) [22,23]. Assembly-based SAFE-assembly were also designed and prepared as a comparison (Schemes 1c). For this purpose, the DP modification in DP-P(B-DMAEA) was removed and the DP in DP-PEG-PVG was replaced with a lipid molecule, thus changing the force forming the carriers from a coordination bond to a hydrophobic interaction. After intravenous administration, the SAFE-complex efficiently crossed the blood-brain barrier (BBB) and targeted neurons under the guidance of RVG (peptides derived from rabies virus glycoproteins) the hydrophobic effect of fatty chains [24–26]. SPIONs-enhanced magnetic resonance imaging (MRI) traced this process *in vivo* [27,28]. In diseased neurons, high levels of ROS stimulated siKeap1 release to mediate the smart clearance of ROS and alleviate PD. While the SAFE-complex metabolized in the liver down-regulated pathological ROS and alleviated CLI (Scheme 1d).

## 2. Materials and methods

### 2.1. Materials

4-Cyano-4-(dodecylsulfanylthiocarbonyl)sulfanylpentanoic acid (CTA, 97%), 2-(dimethylamino) ethyl acrylate (DMAEA, 98%), 4-(bromomethyl)phenylboronic acid (BPA, 98%), superdry dimethyl sulfoxide

(DMSO, 99.7%), and N, N-diisopropylethylamine (DIEA, 99%) were purchased from J&K Scientific Ltd. 4-Biphenylcarboxylic acid (98%), N-(3-dimethylaminopropyl)-N'-ethylcarbodiimide hydrochloride (EDC·HCl, 98%), N-hydroxysuccinimide (NHS, 98%) and N,N-diisopropylethylamine (DIEA, 99%) were purchased from TCI. Iron (III) acetylacetonate (98%), oleic acid (99%), and benzyl ether (98%) were purchased from Alfa Aesar. 4-(2-Aminoethyl)benzene-1,2-diol (DP, 98%) was purchased from Macklin. 1,2-dioleoylsn-glycero-3-phosphoethanolamine-*n*-[poly(ethyleneglycol)]2000-maleimide (DSPE-PEG-Mal) was purchased from Shanghai Advance Vehicle Technology Pharmaceutical L.T.D. Dopamine-[poly(ethyleneglycol)]2000-maleimide (DP-PEG-Mal) was purchased from Ponsure Biological. RVG-cysteine peptide (RVG-SH, YTIWMPENPRPGTDCDIFNRSRGRKASNGC) [29,30] was obtained from Guoping Pharmaceutical. Carbon tetrachloride (CCl<sub>4</sub>, 99%) and olive oil (medical grade, Ph Eur) was purchased from Innochem. 2,2'-Dicyano-2,2'-azopropane (AIBN, 98%) and Hydrogen peroxide solution (H<sub>2</sub>O<sub>2</sub>, 30 wt%) were purchased from Aladdin Industrial Corporation. (3-(4,5-Dimethylthiazol-2-yl)-2,5-diphenyltetrazolium bromide (MTT, 98%) and 4',6-diamidino-2-phenylindole dihydrochloride (DAPI, 98%) were purchased from Sigma-Aldrich. LysoTracker Red was obtained from Thermo Fisher Scientific Inc. 1-Methyl-4-phenylpyridinium iodide (MPP<sup>+</sup>, 98%) and 1-Methyl-4-phenyl-1,2,3,6-tetrahydropyridine hydrochloride (MPTP) was purchased from Sigma-Aldrich. N,N-Dimethylformamide (DMF), chloroform, tetrahydrofuran (THF), DMSO, and methanol were of analytical grade and purchased from Macklin.

### 2.2. Preparation of SPIONs

SPIONs were synthesized by high-temperature thermal decomposition based on previous studies conducted in our lab [31]. 4-Biphenylcarboxylic acid (0.400 g), iron (III) acetylacetonate (0.706 g), oleic acid (1.270 g), and benzyl ether (19 mL) were mixed in a three-neck round bottom flask. The solution was heated to 120 °C and kept in an N<sub>2</sub> atmosphere for 15 min. Then the mixture solution was heated to 290 °C at a rate of 20 °C/min and aged for 90 min. After the solution was cooled, the solution was washed with methanol, and SPIONs with better magnetic properties were selected and dissolved in chloroform.

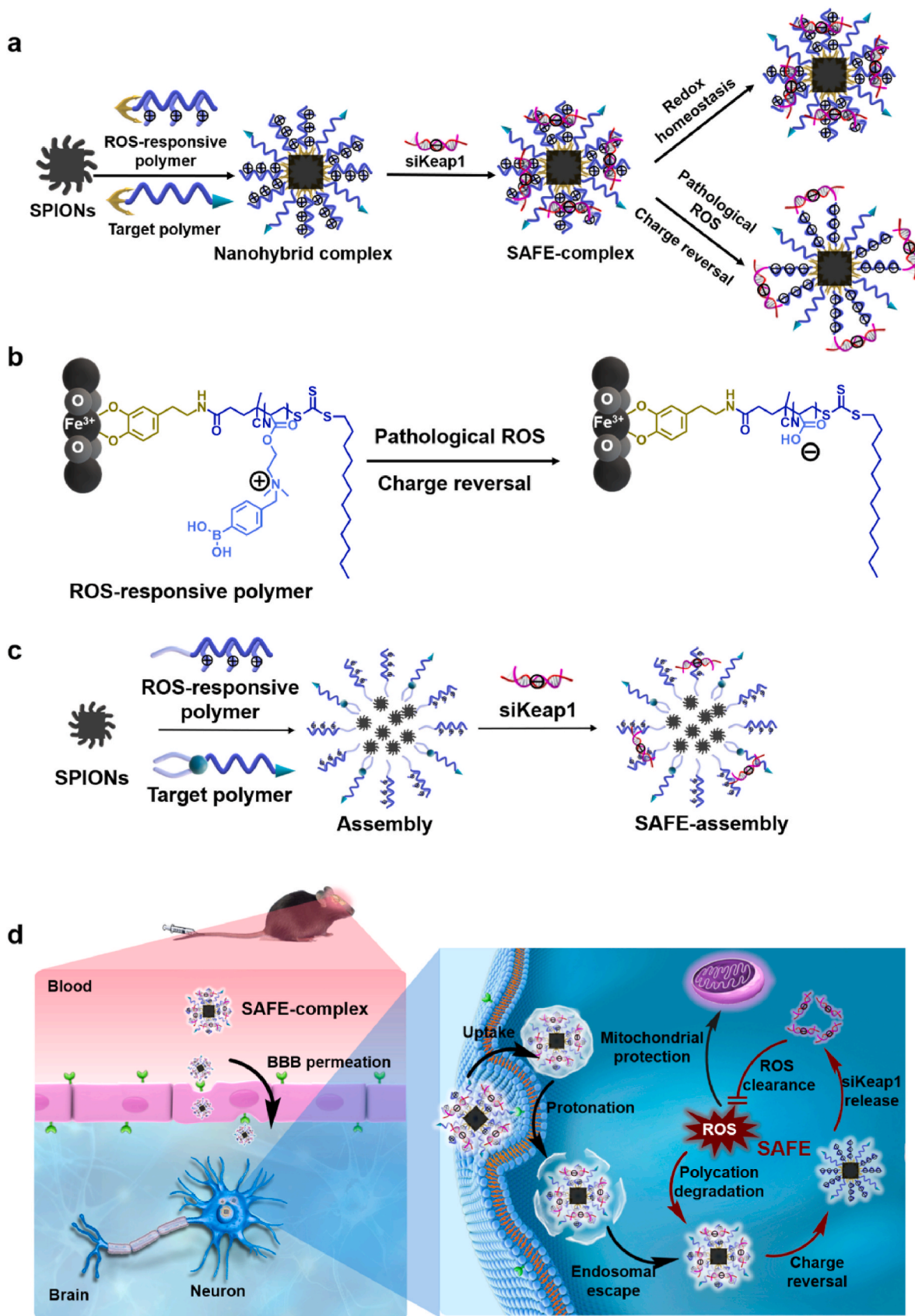
### 2.3. Synthesis of DP-P(B-DMAEA) polymers

#### 2.3.1. Synthesis of PDMAEA

PDMAEA was synthesized by the reversible addition-fragmentation chain transfer (RAFT) polymerization. Briefly, DMAEA (5000 mg), CTA (282 mg), and AIBN (47 mg) were dissolved in DMF (5 mL), and the above solution was then added to a dried Schlenk flask. The Schlenk flask was degassed by three freeze-pump-thaw cycles and recharged with nitrogen, and the reaction mixture was stirred at 70 °C for 24 h. The resulting liquid was dialyzed in a cellu SepH1-membrane (MWCO 3500) against DMF and deionized water sequentially to remove the unreacted monomers and impurities. After 48 h of dialysis, the liquid was freeze-dried to get the final product PDMAEA. The <sup>1</sup>H NMR (Bruker 600 MHz, DMSO-d<sub>6</sub>, δ ppm) characterized the product.

#### 2.3.2. Synthesis of DP-PDMAEA

DP-PDMAEA was synthesized through a condensation reaction. The modified DP could anchor the polymer to the surface of SPIONs by forming a coordination bond with SPIONs through its catechol moiety. In brief, 1 mmol of PDMAEA, 2 mmol of DIEA, 1.2 mmol of EDC·HCl, and 1.2 mmol of NHS were mixed in superdry DMSO and stirred for 90 min. Then, 1.2 mmol of DP was dissolved in superdry DMSO and added dropwise to the above solution. The solution reacted at room temperature for 72 h. The products were placed in a cellu SepH1-membrane (MWCO 3500) and dialyzed for 72 h. After freeze-drying, the DP-PDMAEA was obtained. These products were verified by <sup>1</sup>H NMR (Bruker 600 MHz, DMSO-d<sub>6</sub>, δ ppm).



**Scheme 1.** The Schematic diagram of the preparation of SAFE-complex and therapeutic mechanism. **a** Schematic diagram of the preparation process of the SAFE-complex and smart release of siKeap1. **b** Schematic diagram of the molecular mechanism of ROS-responsive charge reversal of the SAFE-complex. **c** Schematic diagram of the preparation process of SAFE-assembly. **d** Schematic diagram of the SAFE-complex for treatment by the SAFE strategy. The red arrows indicated the mechanism of smart antioxidant function enhancing.

### 2.3.3. Synthesis of DP-P(B-DMAEA)

The introduction of BPA conferred ROS sensitivity to the polymer. DP-PDMAEA (180 mg) and BPA (270 mg) were dissolved in 10 mL of DMF and stirred at room temperature for 24 h. The resulting liquid was dialyzed in a cellulose SepH1-membrane (MWCO 3500) against DMF and deionized water sequentially and then freeze-dried to obtain the final product DP-P(B-DMAEA). The  $^1\text{H}$  NMR (Bruker 600 MHz,  $\text{CD}_4\text{O}$ ,  $\delta$  ppm) was carried out to characterize the obtained product.

### 2.3.4. Synthesis of DP-PEG-RVG

The modification of RVG offered BBB permeation and neuronal targeting capabilities to the polymer. RVG-SH peptide (sequence YTIWMPENPRPGTDCIFITNSRGRKASNGC, 80 mg) and DP-PEG-Mal polymers (50 mg) were dissolved in DMF and shaken vigorously at room temperature for 24 h. After that, the solution was placed in a cellulose SepH1-membrane (MWCO 3500) and dialyzed for 3 h to obtain the final product. The  $^1\text{H}$  NMR (Bruker 600 MHz,  $\text{CD}_4\text{O}$ ,  $\delta$  ppm) was carried out to characterize the obtained product. The matrix-assisted laser desorption/ionization time-of-flight mass spectrometry (MALDI-TOFMS) was carried out to characterize the obtained product.

### 2.3.5. Synthesis of P(B-PDMAEA)

To prepare assembly-based carriers as a contrast, the polymer P(B-PDMAEA) without DP modification was synthesized. The hydrophobic fatty chains on P(B-PDMAEA) contribute to the formation of the assembly. PDMAEA (90 mg) and BPA (135 mg) were dissolved in 10 mL DMF and stirred at room temperature for 24 h. The resulting liquid was dialyzed in a cellulose SepH1-membrane (MWCO 3500) against DMF and deionized water sequentially and then freeze-dried to obtain the final product DP-P(B-DMAEA). The  $^1\text{H}$  NMR (Bruker 600 MHz,  $\text{CD}_4\text{O}$ ,  $\delta$  ppm) was carried out to characterize the obtained product.

### 2.3.6. Synthesis of DSPE-PEG-RVG

DSPE-PEG-RVG was synthesized to participate in the assembly-based carriers and to confer them BBB penetration and neuronal targeting functions. RVG-SH (80 mg) and DSPE-PEG-Mal (50 mg) were dissolved in DMF and shaken vigorously at room temperature for 24 h. After that, the solution was placed in a cellulose SepH1-membrane (MWCO 3500) and dialyzed for 3 h to obtain the final product. The MALDI-TOFMS was carried out to characterize the obtained product.

## 2.4. Preparation of the SAFE-complex

DP-P(B-DMAEA) (8 mg) and DP-PEG-RVG (2 mg) were dissolved in a methanol solution (2 mL). SPIONs (1 mg) dissolved in chloroform (8 mL). The two solutions were mixed and shaken vigorously at room temperature for 6 h. The solvents were evaporated to dryness in the  $\text{N}_2$  and dried in a vacuum drying oven. The crude product was dissolved in appropriate water, centrifuged at 3000 rpm for 10 min, and removed the precipitate. Then, the free polycations were removed by dialysis (MWCO 14000) to obtain the nanohybrid complexes. The SAFE-complex was prepared by adding siKeap1 to the nanohybrid complexes solution at various mass ratios for 1 h at room temperature. Non-targeted nanohybrid complexes were prepared using the same procedure but with DP-PEG-Mal instead of DP-PEG-RVG. SAFE-complex was sterilized by sterile syringe filter (Millex®, pore size 0.22  $\mu\text{m}$ , diam. 33 mm, sterile, hydrophilic) for subsequent cell and animal experiments.

## 2.5. Preparation of the SAFE-assembly

P(B-PDMAEA) (8 mg) and DSPE-PEG-RVG (2 mg) were dissolved in DMSO solution (200  $\mu\text{L}$ ). This mixture was dropwise added into deionized water (2 mL) under vigorous stirring. Then, the solution continued to be stirred for 10 min. Hydrophobic SPIONs (1 mg) were dissolved in

THF. THF-containing SPIONs were added dropwise to the above solution under the ultrasonic environment. After that, the solution continued to be sonicated for 30 min. This solution was dialyzed for 10 h to remove organic solvents to obtain the assemblies. The SAFE-assembly were prepared by adding siKeap1 to the assemblies solution at various mass ratios for 1 h at room temperature. SAFE-assembly was sterilized by sterile syringe filter (Millex®, pore size 0.22  $\mu\text{m}$ , diam. 33 mm, sterile, hydrophilic) for subsequent cell and animal experiments.

## 2.6. Physicochemical characterization of nanoparticles

### 2.6.1. Size and zeta potential of nanoparticles

The sizes and zeta potentials of the nanoparticles were measured by dynamic light scattering (DLS) at 25 °C. Moreover, the stability of nanoparticles was also evaluated by measuring particle sizes and zeta potentials. The nanoparticles were dissolved in PBS (0.01 mM, pH 7.2–7.4) at 4 °C for a given time, and the size of the nanoparticles was measured by DLS at 25 °C to evaluate their storage stability. The nanoparticles were dissolved in medium containing 10% fetal bovine serum (FBS) at 37 °C for a given time, and then the size of the nanoparticles was measured by DLS at 25 °C to evaluate their serum stability. The nanoparticles were freeze-dried and re-solubilized with PBS (0.01 mM, pH 7.2–7.4), and the size and  $\zeta$ -potential of the nanoparticles were detected by DLS at 25 °C to evaluate their freeze-drying stability.

### 2.6.2. Transmission electron microscopy (TEM) morphology characterization

According to the TEM sample preparation procedure, we placed a drop of nanoparticles on the carbon-coated copper grid and immersed it in a 2% phosphotungstic acid solution (pH 7.0) for 30 s. The preparations were observed with a transmission electron microscope (JEM 1200EX) at an acceleration voltage of 100 kV.

### 2.6.3. Transverse relaxation property measurement

The transverse relaxation property of the SAFE-complex without RVG and the SAFE-assembly was measured by a 1.5 T Magnetic Resonance Analyzer (Bruker, minispec mq60).

### 2.6.4. Fourier transform infrared (FTIR) characterization

The DP-PEG-RVG, DP-P(B-DMAEA), and the SAFE-complex were addressed as KBr pellets. Then the infrared absorptions of these samples were measured by a Fourier transform infrared spectrophotometer (JASCO FTIR-200).

## 2.7. Cell culture

SH-SY5Y, immortalized human astrocytes and immortalized human brain microvascular endothelial cells (hCMEC/D3) were cultured in Dulbecco's modified eagle medium (DMEM) supplemented with 10% FBS and 1% penicillin/streptomycin. They were incubated at 37 °C in 5%  $\text{CO}_2$ .

## 2.8. Assay of cell toxicity

$1 \times 10^4$  SH-SY5Y cells were seeded into 96-well plates and incubated with different concentrations of the SAFE-complex and the SAFE-assembly for 24 h. Then, MTT (20  $\mu\text{L}$ , 5 mg/mL) was added to each well and incubated for another 4 h. The medium was aspirated gently from each well, and 100  $\mu\text{L}$  of DMSO was added. The absorbance at 490 nm was measured using a Microplate reader (Tecan, Switzerland). The following formula calculated the relative cell viabilities:

$$\text{Cell viability (\%)} = [\text{OD}(\text{sample})]/[\text{OD}(\text{control})] \times 100\%.$$

## 2.9. Transcytosis across the *in vitro* BBB model

In order to simulate the blood-brain barrier *in vivo*, the hCMEC/D3 and immortalized human astrocytes were cultivated in the upper and lower layers of the Transwell insert, respectively. After the resistance value reached  $200 \Omega \text{ cm}^2$  of the Transwell insert, SH-SY5Y cells were seeded in the lower plate. Different nanoparticles loaded with Cy5-siRNA were added into the Transwell insert for 12 h. After that, the Transwell insert and lower plate were detected by PerkinElmer IVIS spectrum.

## 2.10. Endosomal escape of the SAFE-complex

$1 \times 10^5$  SH-SY5Y cells were seeded in 35 mm Petri dishes (Cellvis) for 24 h and then incubated with the SAFE-complex including  $1 \mu\text{g}$  of FAM-siRNA for 2 and 4 h at  $37^\circ\text{C}$ , respectively. The cells were washed three times with PBS, followed by staining with LysoTracker Red. After washing with PBS, the cells were fixed with 4% paraformaldehyde. Finally, the nucleus was stained with DAPI for 15 min at  $37^\circ\text{C}$ . The fluorescence images were taken by CLSM (Zeiss Co., Germany).

## 2.11. Release of siKeap1 from nanoparticles *in vitro*

The ROS-responsiveness of nanoparticles was evaluated by agarose gel retardation assay. The SAFE-complex loaded with Cy5-siRNA was incubated at indicated  $\text{H}_2\text{O}_2$  concentrations (0.1 mM, 0.25 mM, 0.5 mM, 0.75 mM, and 1 mM, respectively). Cy5-siRNA were used as controls. Those solutions were then subject to electrophoresis after incubation at  $37^\circ\text{C}$ . The migration of Cy5-siRNA bands was visualized and photographed with a UV Transilluminator at 254 nm. The fluorescence images of Cy5-siRNA bands were measured by PerkinElmer IVIS spectrum.

CLSM detected the responsive release of siRNA at the cellular level. SH-SY5Y cells were seeded on 35 mm Petri dishes (Cellvis) with a density of  $5 \times 10^4$  cells per well and cultured for 24 h. Then, the medium containing 1 mM  $\text{MPP}^+$  was added to the dishes. After 24 h, the cells were incubated with Cy5 labeled the SAFE-complex, containing  $1 \mu\text{g}$  of FAM-siRNA. After culturing for 2 h and 4 h, the medium was discarded, and the nuclei were stained with DAPI after washing with PBS three times. The fluorescence images were taken by CLSM (Zeiss Co., Germany). The cells were treated identically for the control experiments, except no  $\text{MPP}^+$  was provided.

## 2.12. Investigation of keap1-Nrf2-ARE pathway activation

$1 \times 10^5$  SH-SY5Y cells were seeded into 6-well plates and incubated until 90% confluence was achieved. Then, the medium containing 1 mM  $\text{MPP}^+$  was added to the dishes. After 24 h, the cells were respectively incubated with the SAFE-complex and the SAFE-assembly for another 24 h. Cells were then collected by scraping and lysed with RIPA lysis solution. Finally, the expression levels of Keap1 and Nrf2 were analyzed by western blot.

## 2.13. *In vitro* ROS scavenging ability of the SAFE-complex

A DCFH-DA probe monitored the generation of ROS. Briefly,  $5 \times 10^4$  SH-SY5Y cells were seeded in 35 mm Petri dishes (Cellvis) for 24 h. Then, the medium containing 1 mM  $\text{MPP}^+$  was added to the dishes. After 24 h, the cells were respectively incubated with the SAFE-complex and the SAFE-assembly for another 24 h. After that, the cells were washed thrice with PBS and stained with a DCFH-DA probe. After washing with PBS, the cells were fixed with 4% paraformaldehyde. Finally, the nucleus was stained with DAPI for 15 min at  $37^\circ\text{C}$ . The fluorescence images were taken by CLSM (Zeiss Co., Germany).

## 2.14. Detection of mitochondrial membrane potential

The JC-1 fluorescence probe detected the mitochondrial membrane potential. Briefly,  $5 \times 10^4$  SH-SY5Y cells were seeded in 35 mm Petri dishes (Cellvis) for 24 h. Then, the medium containing 1 mM  $\text{MPP}^+$  was added to the dishes. After 24 h, the cells were respectively incubated with the SAFE-complex and the SAFE-assembly for another 24 h. After that, the medium was removed, and a JC-1 probe ( $5 \mu\text{g}/\text{mL}$ ) was added to each well. They were incubated for 15 min and washed three times with PBS. Finally, the fluorescence images were taken by CLSM (Zeiss Co., Germany).

## 2.15. Animals

8-week-old mice (C57BL/6, male) and 8-week-old rats (SD, male) were purchased from the Academy of Military Medical Sciences of China. All animal experiments were carried out in accordance with guidelines evaluated and approved by Institutional Animal Care and Use Committee.

## 2.16. Serum chemistry and blood routine measurement

8-week-old male SD rats were injected intravenously with PBS and SAFE nanoparticles, respectively. siKeap1 was administered at a 2.5 mg/kg dose every 3 days for 2 doses. Whole blood samples were collected for serum chemistry analysis and routine blood tests. Blood biochemistry indexes were measured by Mindray BS-420 automatic biochemical analyzer. Routine blood was measured by the Sysmex XE-2100 Fully Automatic Hematology Analyzer.

## 2.17. Evaluation of therapeutic efficacy of MPTP-induced PD model mice *in vivo*

### 2.17.1. The construction of acute PD model mice

Acute PD model mice were constructed with reference to the previous methods of Kim's lab and our lab [32,33]. MPTP (30 mg/kg) was injected intraperitoneally into experimental mice of 6 to 8-week-old male mice (C57BL/6) for seven consecutive days to construct PD model mice. Behavior experiments proved the successful construction of PD model mice.

### 2.17.2. Brain accumulation of SAFE nanoparticles *in vivo*

For the brain accumulation of nanoparticles, PD mice were injected with Cy7 labeled nanoparticles (the SAFE-complex without RVG, the SAFE-assembly, and the SAFE-complex) containing  $10 \mu\text{g}$  of siRNA ( $n = 3$ ). For the distribution of siRNA *in vivo*, the mice were injected with nanoparticles containing  $10 \mu\text{g}$  of Cy5 labeled siRNA. The KODAK *In-Vivo* Imaging System FX Pro investigated the fluorescence absorption *in vivo* imaging system.

### 2.17.3. SAFE nanoparticle-enhanced MRI of the brain *in vivo*

The SAFE-assembly and the SAFE-complex were injected into PD mice via the tail vein at a concentration of  $200 \mu\text{mol Fe}/\text{kg}$  body weight. Mice were anesthetized with 2.5% isoflurane after 6 h, and then isoflurane was reduced to 1% to maintain anesthesia for the MRI study. It was carried out at the 7 Tesla MRI system. The imaging parameters were  $100 \mu\text{m}$  isotropic spatial resolution; TR = 80 ms; TE = 12.3 ms; BW = 75 kHz; FA =  $20^\circ$ .

### 2.17.4. Treatment schedule of MPTP-induced PD model mice

PD mice were randomly grouped, in which wild-type (WT) mice and PD control group were not treated ( $n = 5$ ). Other groups were intravenously injected with different kinds of the SAFE nanoparticles (the SAFE-complex without RVG, the SAFE-assembly, and the SAFE-complex) containing siKeap1 (1 mg/kg) every three days for 10 times.

### 2.17.5. Behavioral test of SAFE nanoparticle-treated PD mice

The open field test was carried out with reference to the previous methods of our lab [34]. Individual mice were positioned in the middle of an open field box (48 cm × 48 cm), and the spontaneous motor movements of each mouse were recorded (n = 3). The computer software automatically evaluated the following parameters: the total traveled distance and the total rest time. The pore test was also carried out with reference to the previous methods of our lab [23]. The mice were then put upright on a 50 cm high pole, and we timed how long it took them to complete the distance in order to evaluate the mice's ability to coordinate their movements (n = 3).

### 2.17.6. In vivo ROS scavenging ability of the SAFE nanoparticles

The frozen sections of the substantia nigra region in each group were stained with ROS fluorescence staining, and the nuclei were stained with DAPI (n = 3). The level of ROS reflected by the ROS fluorescence staining was observed under a microscope (DS-U3, NIKON). To quantitatively analyze the changes in ROS expression levels, the tissue ROS detection kit was used to detect the ROS changes in the substantia nigra region of each brain.

### 2.17.7. Activity of mitochondrial complex I

The Mitochondrial Complex I Activity Assay Kit evaluated the activity of mitochondrial complex I. Mice brain samples were homogenized and processed according to the manufacturer's instructions (n = 3). A microplate reader detected absorbance, and mitochondrial complex I activity was calculated.

### 2.17.8. Detection of MDA content

According to the manufacturer's instructions, a lipid peroxidation assay kit quantified malondialdehyde (MDA) content in fresh mice brains (n = 3). MDA-thiobarbituric acid adduct's appearance rates were quantified colorimetrically at 450 nm, 532 nm, and 600 nm using a spectrophotometer.

### 2.17.9. Activity of antioxidant enzymes

The activity of antioxidant enzymes, including superoxide dismutase (SOD), catalase (CAT), and glutathione peroxidase (GSH-Px), was detected by the kit method. Fresh brain samples were homogenized in a buffer, and supernatants and precipitates were separated by centrifugation (n = 3). The resulting supernatants were used to measure SOD, CAT, and GSH-Px activities according to the instructions provided with each kit.

### 2.17.10. Immunostaining analysis

Fresh brain samples of all groups were obtained and fixed in 4% formalin for 45–60 min, followed by storage in 70% alcohol (n = 3). The tissues were processed routinely, paraffin-embedded, and cut into 5-μm thick sections. Immunohistochemical staining was performed with antibodies against tyrosine hydroxylase (TH) using mouse monoclonal anti-TH. Organs (heart, liver, spleen, lung, and kidney) from mice in each group were sectioned and stained by hematoxylin and eosin-stained (H&E) staining for tissue morphology evaluation.

## 2.18. Evaluation of therapeutic efficacy of CCL<sub>4</sub>-induced CLI model mice in vivo

### 2.18.1. Treatment schedule of CCL<sub>4</sub>-induced CLI model mice

The CLI model mice were constructed with reference to the previous method of Tacke's lab [35]. A mixture of CCL<sub>4</sub> (0.6 mL/kg) and olive oil (2.4 mL/kg) was injected intraperitoneally twice a week for a total of 12 injections into 8-week-old C57BL/6 male mice to construct CLI mice. Then, CLI mice were randomly grouped (n = 5), in which WT mice and CLI control group were not treated. Other groups were intravenously injected with different kinds of SAFE nanoparticles (the SAFE-complex

without RVG, the SAFE-assembly, and the SAFE-complex) containing siKeap1 (1 mg/kg) every three days for 10 times.

### 2.18.2. Evaluation of liver injury level

Three days after the last dose, whole blood was collected from mice (n = 5). The Mindray BS-420 automatic biochemical analyzer was used to detect glutathione (ALT) and glutamic acid aminotransferase (AST). Mouse body weight was recorded. Mice livers were isolated and washed with saline. After aspiration, the liver weight was recorded. The mouse liver index was calculated.

$$\text{Liver index (\%)} = \frac{\text{weight}_{\text{liver}} (\text{g})}{\text{weight}_{\text{mouse}} (\text{g})} \times 100\%$$

### 2.18.3. Immunostaining analysis

A portion of mouse liver was fixed in 4% paraformaldehyde solution for 45–60 min, paraffin-embedded, and cut into 5 μm-thick sections for H&E and Masson staining, respectively (n = 3). A portion of mouse liver was prepared as frozen sections for ROS, anti-Keap1, and anti-Nrf2 staining, respectively.

## 2.19. Statistical analysis

All data were expressed as mean ± SD (n = 3 or 5). Statistical significance was analyzed using a two-tailed *t*-test (\**p* < 0.05, \*\**p* < 0.01, \*\*\**p* < 0.001). Statistical analysis was carried out using GraphPad Prism 8.0.1 software. The electropherograms and WB images were quantified by Image J software. Confocal images were quantified by Image-Pro Plus software.

## 3. Results and discussion

### 3.1. The preparation and characterization of the SAFE-nanoparticles

The synthetic route of drug-loaded polymers DP-P(B-DMAEA) was shown in Fig. S1, and the <sup>1</sup>H NMR spectra identified the chemical structures of DP-P(B-DMAEA) and its intermediate products (Fig. S2). The synthetic route of targeted polymer DP-PEG-RVG was shown in Fig. S3, and the DP-PEG-RVG was identified by MALDI-TOFMS (Fig. S4). As a comparison, we also synthesized amphiphilic drug-loaded polymer P(B-DMAEA) (Figs. S5 and S6) and amphiphilic targeted polymer DSPE-PEG-RVG (Figs. S7 and S8) to prepare self-assembled carriers. The SPIONs prepared by high-temperature thermal decomposition were cubic with a length of about 18 nm and were homogeneous in size and shape (Fig. S9). DP-P(B-DMAEA) and DP-PEG-RVG were anchored on the surface of SPIONs through the coordination of catechol with iron oxide to form nanohybrid complexes. In the FTIR spectrum of nanohybrid complexes, the stretching vibration peaks of the hydroxyl group at 3300–3500 cm<sup>-1</sup> and carbonyl group at 1705–1725 cm<sup>-1</sup> proved that DP-P(B-DMAEA) was modified on the surface of SPIONs. 1115 cm<sup>-1</sup> was the stretching vibration peak of C–O–C, which proved that DP-PEG-RVG was also modified on the surface of SPIONs (Fig. 1a). After anchoring the polymer, the nanoparticles were transformed from the organic phase into the aqueous phase, making them feasible to deliver nucleic acid drugs (Fig. 1a). As a comparison, the assembly-based SAFE nanoparticles (SAFE-assembly) were prepared by a self-assembly method (Scheme 1c). The homogeneous and monodisperse nanohybrid composite proved that the preparation process was controllable (Fig. S10a). In contrast, the assemblies were heterogeneous and polydisperse (Fig. S10b). For the carriers, the form of lyophilized powder is conducive to its long-term stable storage. Therefore, it is crucial to have freeze-drying stability. Neither the nanohybrid complexes' size nor zeta potential changed significantly after freeze-drying-redissolution. In contrast, the diameter of the assemblies was increased to 2.4 times that

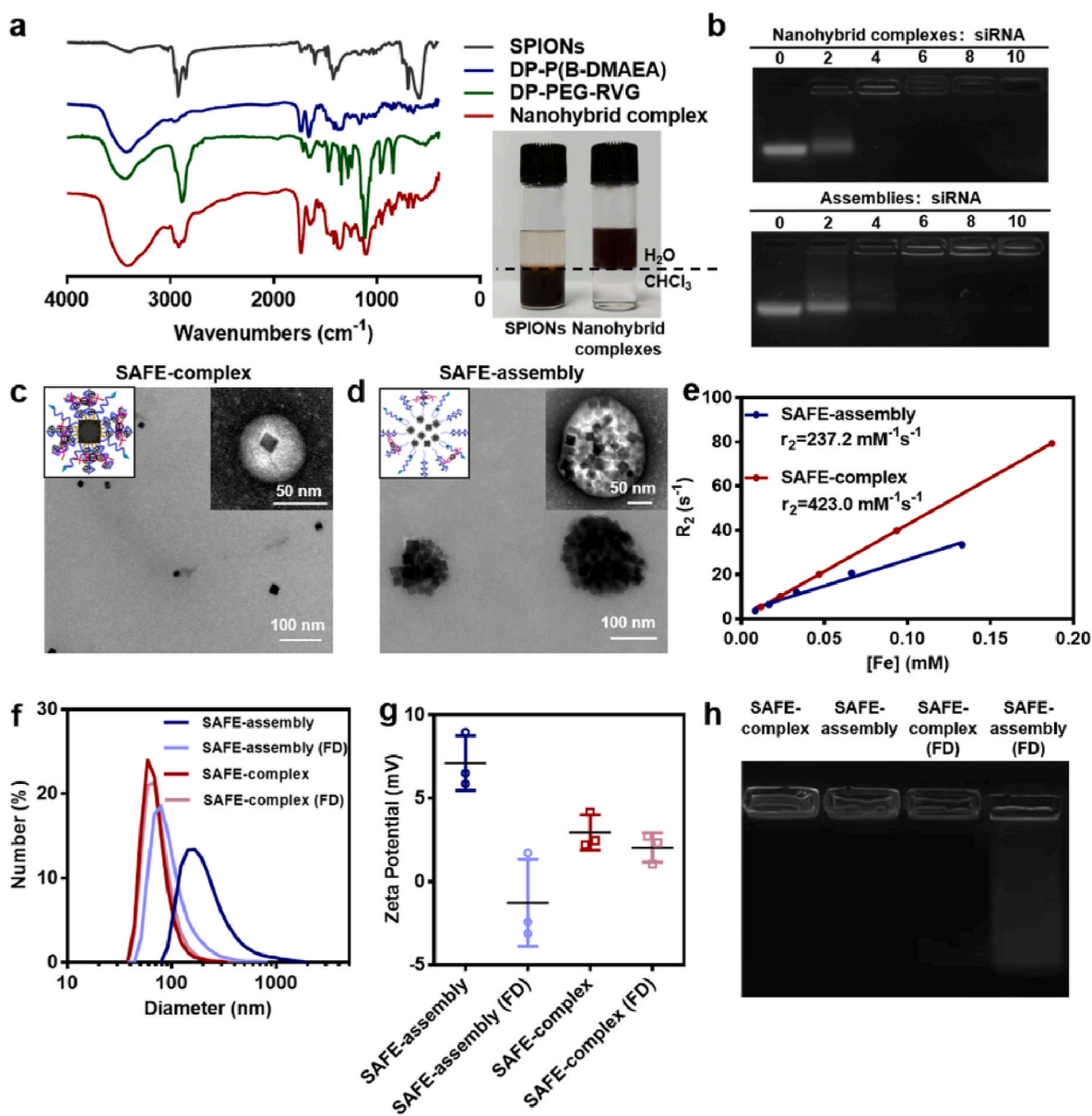


**Fig. 1.** Characterization of the nanoparticles. **a** The FTIR spectra. The inset showed the distribution of SPIONs and nanohybrid complexes in the mixture of H<sub>2</sub>O and CHCl<sub>3</sub> before and after anchoring polymers. **b** Agarose gel electrophoresis after siRNA loading. **c** The TEM image of the SAFE-complex. Scale bar: 100 nm. The inset was TEM images after negative staining. Scale bar: 50 nm. **d** The TEM image of the SAFE-assembly. Scale bar: 100 nm. The inset was TEM images after negative staining. Scale bar: 50 nm. **e** Relaxation rate testing of siRNA delivery systems. **f** Particle size change of the drug delivery systems before and after freeze-drying. FD represented freeze-dried and redissolved nanoparticles. **g** Changes in the zeta potential of drug delivery systems before and after freeze-drying. Data were presented as the mean  $\pm$  SD ( $n = 3$ ). **h** Agarose gel electrophoresis of the drug delivery system before and after freeze-drying.

before freeze-drying, and the zeta potential was significantly reduced compared to that before freeze-drying, making it unsuitable for nucleic acid drug loading and *in vivo* delivery (Fig. S11). These results demonstrated that the controllable prepared nanohybrid complexes were superior to the assemblies in terms of homogeneity and stability.

Both nanohybrid complexes and assemblies could load siRNA by electrostatic adsorption. As shown in Fig. 1b, when the mass ratio of the nanohybrid complex:siRNA was 4:1, nanohybrid complexes could completely adsorb siRNA. By contrast, when the mass ratio of assembly:siRNA was 6:1, the assemblies could completely adsorb siRNA. After loading siRNA, both the SAFE-complex and the SAFE-assembly morphology did not change significantly. The SAFE-complex remained in a homogeneous monodisperse (Fig. 1c). The SAFE-assembly showed an inhomogeneous polydispersity (Fig. 1d). The relaxation rate of the SAFE-complex reached 1.78 times that of the self-assembled SAFE-

assembly (Fig. 1e). The high relaxation rate could be attributed to replacing hydrophobic molecules on the SPION of the SAFE-complex with hydrophilic polymers, which could better interact with water molecules. In contrast, the SPIONs in the SAFE-assembly were in the hydrophobic core that repelled water molecules, hindering the interaction of the contrasts with water molecules (Fig. S12). After loading siRNA, the SAFE-complex still exhibited excellent freeze-drying stability compared with the SAFE-assembly, and the particle size and zeta potential showed significant changes after freeze-drying-redissolution (Fig. 1f and g). In addition, the SAFE-complex remained as a homogeneous monodisperse without aggregation after freeze-drying-redissolution (Fig. S13a), while the SAFE-assembly showed severe agglomeration (Fig. S13b). After freeze-drying-redissolution, almost no siRNA was detached from the SAFE-complex, while a large amount of siRNA was detached from the SAFE-assembly (Fig. 1h), which indicated

that the SAFE-complex could be stored stably as a freeze-dried powder, while SAFE-assembly could not. Serum stability is a crucial indicator to evaluate the stability of the carriers during the circulation process. After 96 h of incubation in serum, the size of the SAFE-assembly increased by more than 120%, while the size of the SAFE-complex increased by less than 15% (Fig. S14). In addition, both SAFE-complex and SAFE-assembly have better stability in PBS. These results suggested that the SAFE-complex based on nanohybrid complexes had superior homogeneity, MRI sensitivity, freeze-drying stability, and serum stability compared to the SAFE-assembly based on self-assemblies, which facilitated carrier storage, *in vivo* delivery, and *in vivo* tracing. Besides, the anti-RNAase A degradation property of siRNA was evaluated by agarose gel electrophoresis. As shown in Fig. S15, free siRNA was degraded starting at 0.01  $\mu\text{g}/\mu\text{L}$  of RNAase A and was essentially completely degraded at 12 h. In contrast, siRNA in SAFE-complex started to degrade slightly at 1  $\mu\text{g}/\mu\text{L}$ , which is much lower than the *in vivo* RNAase concentration. Thus, SAFE-complex could protect siRNA from degradation *in vivo*.

### 3.2. Cellular uptake and smart release of siRNA of the SAFE nanoparticles

The SAFE-complex and the SAFE-assembly had excellent biosafety at the cellular level (Fig. S16). Crossing the BBB and targeting neurons are necessary for SAFE nanoparticles to treat PD. To investigate the influences of structural and ligand modifications on the siRNA delivery to PD lesions by SAFE nanoparticles, we prepared the SAFE-complex, the SAFE-assembly, and the SAFE-complex without RVG (Fig. 2a). The uptake capacity of these nanoparticles by neurons was firstly examined (Fig. 2b). the SAFE-complex was uptaken most by SH-SY5Y. Whereas, SAFE-complex uptake decreased significantly after RVG pretreatment. Thus, RVG modification and the structure of SAFE-complex themselves promoted the cellular uptake of SH-SY5Y. The cellular-level BBB model was constructed by Transwell (Fig. 2c). BBB-associated hCMEC/D3 cells and immortalized human astrocytes were cultured in the upper and below of the transwell insert, respectively. SH-SY5Y cells were seeded in the lower plate. After adding SAFE nanoparticles in the transwell insert, siRNA uptake was detected in the transwell insert and bottom-plate cells, respectively. As shown in Fig. 2d–h, the SAFE-complex exhibited the highest cellular uptake efficiency in both BBB-associated cells and SH-SY5Y compared to the SAFE-complex without RVG and the SAFE-assembly. This result indicated that RVG modification and stable homogeneous structure together promoted the BBB penetration and neuronal uptake of the siRNA, especially the modification of targeting molecule RVG played a more critical role. To further investigate the mechanism by which targeting molecules promoted transcytosis and uptake, the SAFE-complex were added to the upper layer after the pretreatment of cells with free RVG. The uptake of the SAFE-complex by BBB-associated cells and SH-SY5Y was significantly decreased. It was comparable to the SAFE-complex without RVG in un-RVG pretreated cells, demonstrating that RVG on the surface of the SAFE nanoparticles facilitated BBB permeation and endocytosis through receptor-mediated transcytosis and endocytosis.

Since nucleic acid drugs are degraded by nucleases in endosomes, endosome escape ability is a crucial indicator for evaluating nucleic acid drug carriers [36,37]. The SAFE-complex exhibited an excellent proton sponge effect (Fig. S17), facilitating the protonation of the SAFE-complex in acidic endosomes and thus mediating endosome expansion and breakup. After the SAFE-complex were co-cultured with SH-SY5Y for 2 h, the red fluorescence that labeled endosomes co-localized with the green fluorescence that labeled siRNA, generating a large amount of yellow fluorescence, indicating that SH-SY5Y took up the SAFE-complex through the endosome pathway (Fig. 2i). After 4 h of co-culture, the yellow fluorescence diminished. The co-localization coefficient of red fluorescence with green fluorescence significantly decreased, indicating that siRNA could escape from the endosome

(Fig. S18).

The key to the safe treatment of ROS-related chronic diseases and comorbidities lies in SAFE nanoparticles, while the key to ensuring that SAFE nanoparticles function is the smart release of nucleic acid drugs in pathologically high levels of ROS environments. For this purpose, the ROS-responsive cationic polymer DP-P(B-DMAEA) was synthesized for the electrostatic adsorption and smart release of siKeap1. Pathological high levels of ROS could degrade the phenylboronic acid group on the cationic block of DP-P(B-DMAEA) and accelerate the ester bond hydrolysis, thus converting the cationic blocks into anionic blocks [22] (Fig. S19a). The  $^1\text{H}$  NMR spectra confirmed the ROS response of the DP-P(B-DMAEA) molecular structure after simulating the pathological ROS environment *in vitro* with hydrogen peroxide (Fig. S19b). The siRNA release was quantified by PerkinElmer IVIS spectrum. Briefly, SAFE-complexes loaded with Cy5-siRNA were co-incubated with different concentrations of  $\text{H}_2\text{O}_2$ . After a given time, the released siRNA was separated by electrophoresis and quantified by PerkinElmer IVIS spectrum. As shown in Figs. S20a–S20c, the amount of siRNA was linearly related to the total radiant efficiency of Cy5, and thus could be used for quantification of siRNA bands in electrophoresis. As shown in Figs. S21a, S21b and 2j, at  $\text{H}_2\text{O}_2$  concentrations of 0.5 mM and above, most of the siRNA was released within 1 h. At  $\text{H}_2\text{O}_2$  concentrations of 0.1 and 0.25 mM, a small amount of siRNA was released within 1 h, and most of the siRNA was released within 8 h. This result indicated that the release of siKeap1 was ROS dependent. We further investigated the ability of the SAFE-complex to release siRNA in healthy and diseased neurons. After the SAFE-complex were co-cultured with healthy SH-SY5Y for 2 h and 6 h, the co-localization coefficients of siRNA with the nanohybrid complexes did not change significantly (Figs. S22a–S22c), indicating that siRNA was not released obviously.  $\text{MPP}^+$  is a toxic metabolite of the neurotoxin MPTP.  $\text{MPP}^+$  disrupts mitochondrial function and exacerbates oxidative stress levels when taken up by dopaminergic neurons via the dopamine transporter, resulting in dopaminergic neuronal dysfunction [38,39].  $\text{MPP}^+$ -induced diseased SH-SY5Y cells were co-cultured with the SAFE-complex. Compared to co-culture for 2 h, the co-localization coefficient of the nanohybrid complexes with siRNA was significantly lower at 6 h of co-culture (Fig. 2k and S23), suggesting significant siRNA release. These results demonstrated that the SAFE-complex could be released in diseased neurons on demand, thereby smartly enhancing endogenous antioxidant function.

### 3.3. Pharmaceutical efficacy evaluation of the SAFE nanoparticles at the cellular level

A series of six siRNA sequences targeting both human and mouse Keap1 mRNA were designed by an initial bioinformatics analysis. *In vitro* activity screening was performed in cultured Neuro 2a cells. siKeap1-2367 exhibited the highest silent activity against mouse Keap1 mRNA and was selected for subsequent cellular and animal administration (Table S1). The SAFE-complex exhibited more efficient Keap1 downregulation than the SAFE-assembly, benefiting from superior cellular uptake, endosome escape, and smart release of siRNA. The SAFE-complex-mediated Keap1 downregulation inhibited ubiquitination and degradation of Nrf2, resulting in significant upregulation of Nrf2 levels (Fig. 3a–c). The upregulated Nrf2 translocated to the nuclei to bind to the ARE and activate the Keap1-Nrf2-ARE pathway, thereby protecting cells from ROS damage [10–12]. DCFH-DA fluorescent probes were used to detect intracellular ROS levels. CLSM images showed that SH-SY5Y induced by  $\text{MPP}^+$  significantly increased intracellular ROS levels (Fig. 3d and e, S24a, S24b, and S24e). ROS levels could be reduced after both the SAFE-assembly and the SAFE-complex treatment. In comparison, the SAFE-complex had a more significant ROS clearance effect, and the CLSM results were consistent with the flow cytometry results. (Fig. 3d and e, and S24c–S24e).

Pathologically high levels of ROS exacerbate mitochondrial damage

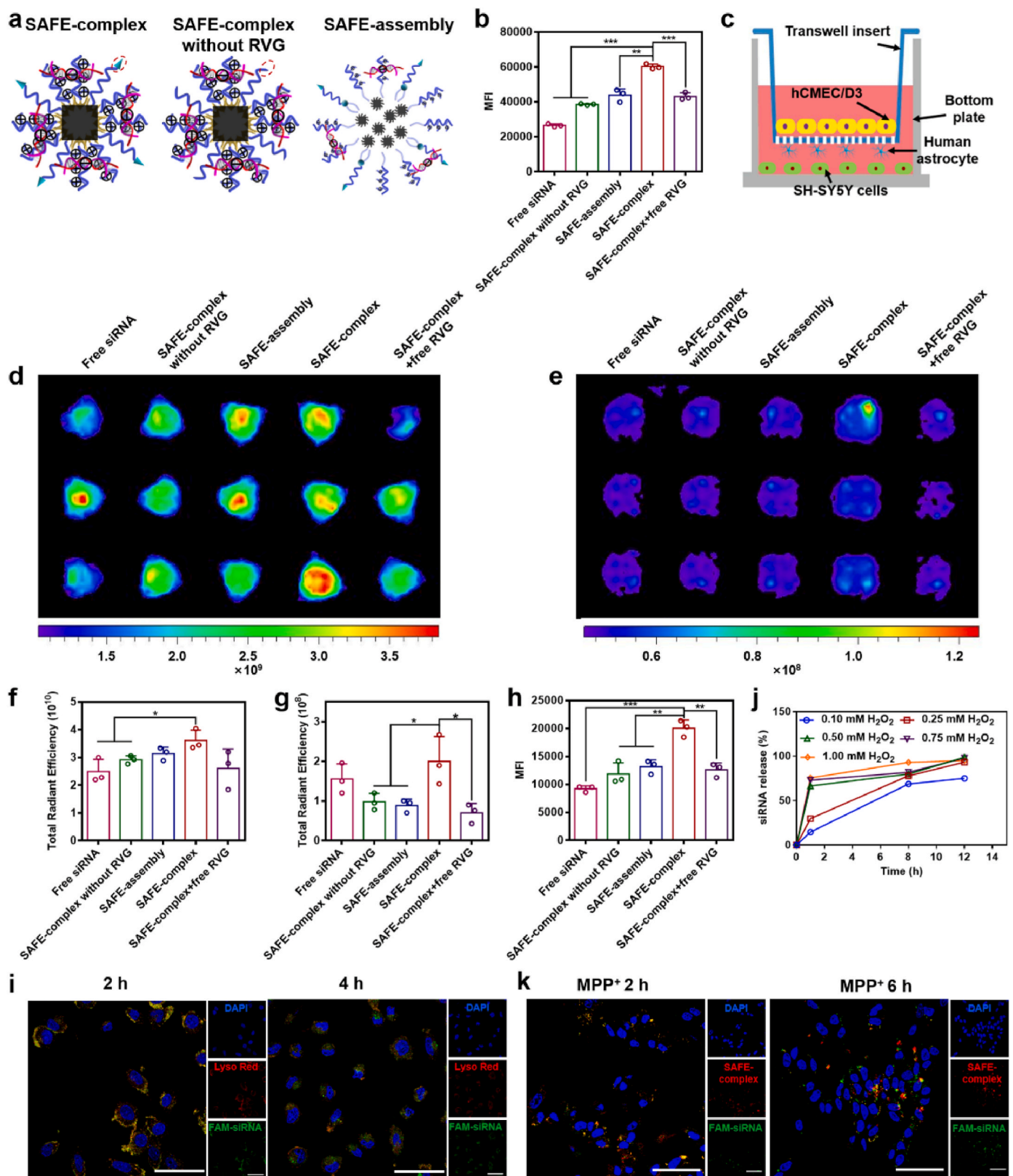


**Fig. 2.** Delivery of the SAFE nanoparticles *in vitro*. **a** Schematic diagrams of the three kinds of SAFE nanoparticles. **b** The uptake of nanoparticles by SH-SY5Y without *in vitro* BBB model that measured by flow cytometer. **c** Schematic diagram of BBB model at the cellular level by Transwell. **d** The fluorescence image of Transwell inserts by PerkinElmer IVIS spectrum. **e** The fluorescence image of bottom plates by PerkinElmer IVIS spectrum. **f** The quantitative result of Fig. 2d **g** The quantitative result of Fig. 2e **h** The uptake of nanoparticles by SH-SY5Y in cellular BBB model that measured by flow cytometer. **i** The CLSM images of the SAFE-complex co-cultured with SH-SY5Y for 2 h and 4 h. Scale bar: 50  $\mu$ m. **j** The siRNA release rate. **k** CLSM images of the SAFE-complex co-cultured with MPP<sup>+</sup>-treated SH-SY5Y for 2 h and 6 h. Scale bar: 50  $\mu$ m. Data were presented as the mean  $\pm$  SD (n = 3). (t-test, \*p < 0.05, \*\*p < 0.01, \*\*\*p < 0.001).

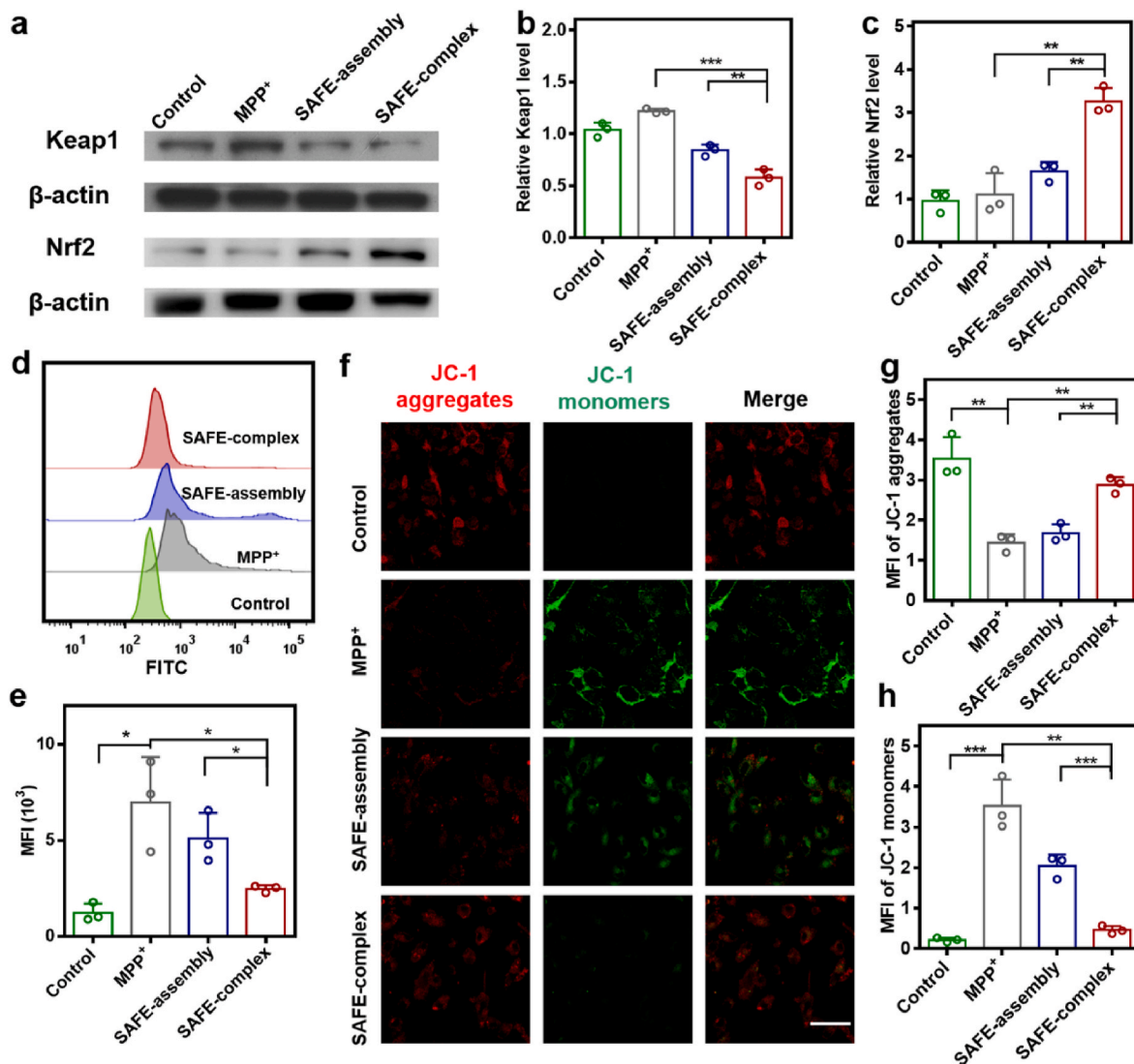


**Fig. 3.** Therapeutic effects of the SAFE nanoparticles *in vitro*. **a** Western blot bands after co-culture with siRNA delivery systems. **b, c** The quantitative results of Fig. 3a. **d, e** The ROS level measured by flow cytometry. **f** The MMP level measured by CLSM. Scale bar: 50  $\mu\text{m}$ . **g-h** MMP measured by CLSM. Scale bar: 50  $\mu\text{m}$ . Data were presented as the mean  $\pm$  SD ( $n = 3$ ). (*t*-test, \* $p < 0.05$ , \*\* $p < 0.01$ , \*\*\* $p < 0.001$ ).

and constitute a significant pathogenesis of PD and organ injuries. Mitochondrial membrane potential (MMP) is one of the most critical indicators for evaluating normal mitochondrial function [40,41]. A high MMP predicts healthy mitochondria. In contrast, a decrease in MMP predicts mitochondrial dysfunction and further mediates autophagy, apoptosis, or necrosis, resulting in various chronic diseases. JC-1 was used to detect MMP in SH-SY5Y. JC-1 is present as aggregates in healthy mitochondria, producing strong red fluorescence. In contrast, JC-1 exists as a monomer in functionally abnormal mitochondrial matrices and emits green fluorescence. MPP<sup>+</sup>-induced increase in ROS levels decreased red fluorescence and enhanced green fluorescence, resulting in severe mitochondrial dysfunction. After the SAFE-assembly treatment, the red fluorescence of JC-1 did not change significantly, while the green fluorescence was significantly diminished, suggesting its weak mitochondrial protective effect. By contrast, the SAFE-complex significantly enhanced the red fluorescence of the JC-1 probe and significantly attenuated its green fluorescence, which recovered to healthy SH-SY5Y levels (Fig. 3f–h). These results suggest the SAFE-complex had better mitochondrial protective effects and could restore dysfunctional mitochondria to healthy levels.

#### 3.4. *In vivo* delivery of the SAFE nanoparticles

The pharmacokinetics of siRNA was measured by PerkinElmer IVIS spectrum. As shown in Figs. S25a and S25b, the half-life of free siRNA is less than 1 h. In contrast, the half-life of siRNA in SAFE-complex was about 2.7 h, which significantly enhanced the half-life of siRNA. Benefiting from a more stable and homogeneous structure, superior siRNA loading ability, and modification of the target molecule RVG, the SAFE-complex already showed excellent BBB penetration ability in a BBB model at the cellular level. Subsequently, KODAK In-Vivo Imaging System FX Pro was employed to monitor the siRNA accumulation process in the brain in real-time (Fig. 4a). The SAFE-complex had the most efficient brain accumulation compared to the SAFE-complex without RVG and the SAFE-assembly. These SAFE nanoparticles were most accumulated in the brain at 2 h (Fig. 4b). After 24 h, mice were sacrificed, and the brains were isolated for ex vivo fluorescence assay. Fig. 4c showed the highest siRNA fluorescence intensity in the brain after intravenous injection of the SAFE-complex, further indicating that the SAFE-complex had superior brain penetration ability. These results were consistent with the results at the cellular level. The excellent serum stability of the SAFE-complex also played a positive role in the

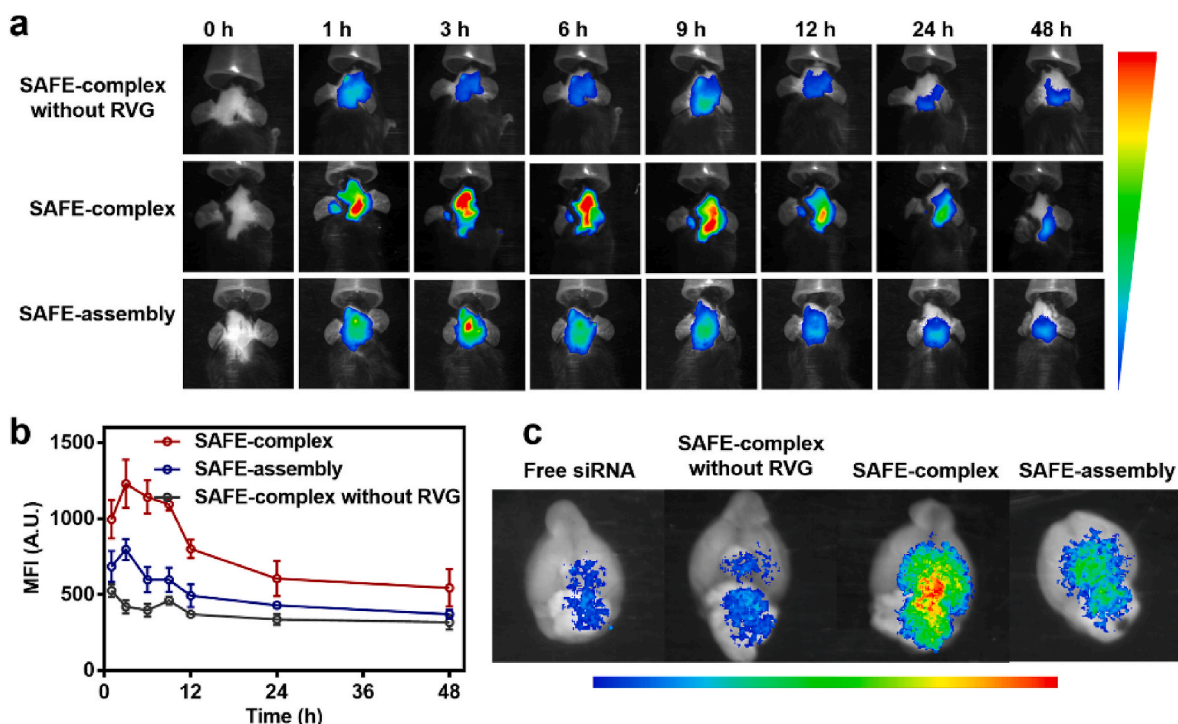


**Fig. 4.** Delivery of the SAFE nanoparticles *in vivo*. **a** *In vivo* real-time fluorescence imaging of siRNA delivery systems in the brains. **b** The quantitative results of Fig. 4a **c** Accumulation of the siRNA delivery system in the brains 24 h after administration. Data were presented as the mean  $\pm$  SD ( $n = 3$ ).

accumulation of siRNA in the brain after intravenous injection. Besides, SAFE-complex promotes BBB penetration and neuronal uptake in three main ways. (1) Targeting ligands. The targeting peptide RVG is highly neurotropic and can specifically bind to nicotinic acetylcholine receptor (nAChR) in the central nervous system, and deliver the conjugated molecules to specific tissues and cells. (2) Physical properties. The SAFE-complex has the small and controllable diameter of about 50 nm, which is conducive to better uptake of the system by cells. (3) Surface chemistry. The outermost side of the SAFE-complex has a hydrophobic alkyl chain, which makes the system cross the cell membrane due to the affinity with the lipid tail when contacting the cell membrane.

MRI offers the advantages of real-time, high resolution, high signal penetration depth, non-invasiveness, and safety. The SAFE-complex provided a higher MRI sensitivity than the SAFE-assembly. In addition, for the SAFE-complex, the contrasts were transformed into nucleic acid drug carriers by anchoring the loading polymers and targeting polymers. It meant that, for the SAFE-complex, the carriers themselves were MRI contrasts. Thus the contrasts could precisely self-trace the accumulation of carriers in the brain by MRI. In contrast, for the SAFE-assembly, the SPIONs were components of the assemblies and thus traced the contrasts themselves rather than the carriers, resulting in artifacts. After intravenous injection, the brain exhibited significant SAFE-complex-enhanced MRI signals. By contrast, only weaker SAFE-assembly-enhanced MRI signals were found in the brain, further confirming the more sensitive MRI and more efficient BBB penetration of the SAFE-complex (Fig. S26).

Biosafety is a prerequisite for the therapeutic application of nucleic acid drugs. SAFE nanoparticles were expected to ensure their biosafety by smartly down-regulating pathologically high levels of ROS. H&E immunohistochemistry sections of major organs, routine blood, and blood biochemistry were used to evaluate the biosafety of the SAFE nanoparticles. After treatment with these SAFE nanoparticles, both routine blood and blood biochemistry remained within normal limits (Tables S2 and S3). Besides, no significant pathological lesion was observed in the main visceral organs (Fig. S27). These results confirmed the biosafety of these SAFE nanoparticles.

### 3.5. PD treatment by SAFE nanoparticles

Acute PD model mice were constructed by continuous intraperitoneal injection of MPTP [32,42,43]. PD mice were treated by intravenous injection once every 3 days for 10 doses (Fig. 5a). The open-field test was used to evaluate the motor ability of PD mice after SAFE nucleic acid therapy (Fig. 5b and S28). After MPTP induction, the total movement distance in the open field significantly shortened, and the resting time was significantly longer, indicating that the motility of the MPTP-induced PD model mice was significantly decreased. After SAFE treatment, all mice showed significant improvement in motor performance. The SAFE-complex had the best motor enhancement effect, while the SAFE-complex without RVG had the worst improvement (Fig. 5c and d). This result was consistent with the siRNA accumulation in the brain. Next, the pole test was used to evaluate the coordination ability of PD mice after SAFE therapy. The coordination ability of MPTP-induced PD mice was significantly reduced compared to WT mice. The coordination ability of PD mice was also significantly enhanced after nucleic acid treatment with all SAFE nanoparticles, and SAFE-complex showed the optimum enhancement (Fig. 5e). It was consistent with the result of the open field. These results demonstrated that SAFE nucleic acid treatment against ROS could improve motor and coordination abilities in PD mice. The enhancement effect was positively correlated with siKeap1 accumulation in the brain.

The gene silencing effects of siRNA against Keap1 were detected by immunofluorescence sections of the substantia nigra region (Fig. S29a). Compared to the SAFE-assembly and the SAFE-complex without RVG, the SAFE-complex maximally downregulated Keap1 expression and increased Nrf2 content in the substantia nigra region (Figs. S29b and S29c). Immunofluorescence sections showed that the Nrf2 upregulation by SAFE nanoparticles activated the Keap1-Nrf2-ARE pathway and thus smartly downregulated ROS level in the substantia nigra region of PD mice (Fig. 6a, S30a–S30c, and 6b). Notably, the SAFE-complex had the best ROS scavenging effect and down-regulated ROS in PD mice to comparable levels in healthy mice, consistent with the results of whole brain ROS levels measured by the ROS detection kit. Antioxidase

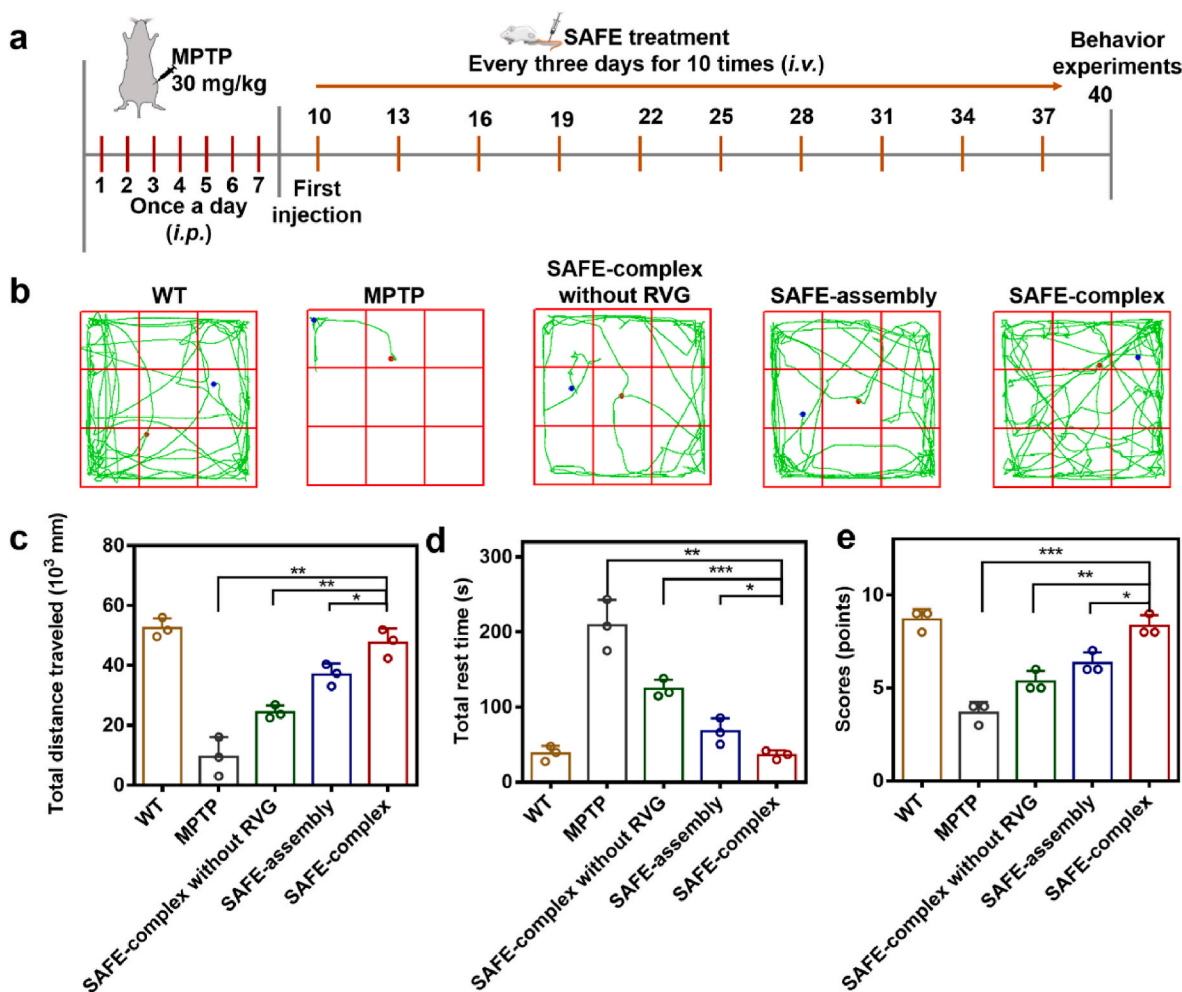


**Fig. 5.** *In vivo* therapeutic effects of safe nanoparticles in PD. **a** The construction and therapeutic schedule of PD model mice. **b** The representative migration routes of mice in the open field. **c, d** The quantitative results of Fig. 5b. **e** The pole test score. Data were presented as the mean  $\pm$  SD ( $n = 3$ ). (*t*-test, \* $p < 0.05$ , \*\* $p < 0.01$ , \*\*\* $p < 0.001$ ).

activities were further examined. SOD, CAT, and GSH-Px activities were significantly increased after SAFE nucleic acid treatment [44,45], and the effect of the SAFE-complex was the most pronounced (Fig. 6c–e). These results indicated that the SAFE-complex contributed to the repair of redox homeostasis through endogenous antioxidant enzymes independent of exogenous antioxidants.

Excess ROS in PD lesions can exacerbate oxidative stress and thus cause oxidative damage to cells and the organism. For example, free radicals mediate the peroxidation of lipid substances to produce toxic MDA [46,47]. Therefore, the MDA content in mouse brains was measured to indicate the degree of intracellular oxidative stress. The MDA was significantly elevated in mouse brains after MPTP induction. SAFE nucleic acid therapy targeting Keap1 could significantly reduce the MDA. The SAFE-complex showed the most efficient oxidative stress relief (Fig. 6f). Peroxides produced by oxidative stress can damage cells by disrupting mitochondrial function. Loss of mitochondrial complex I is one of the markers of PD, and MPTP induces PD symptoms by damaging mitochondrial complex I. SAFE nucleic acid therapy targeting Keap1 elevated the activity of mitochondrial complex I. In particular, the SAFE-complex elevated the activity of mitochondrial complex I in the brains to near normal mice (Fig. 6g). Moreover, the elevated mitochondrial complex I activity promoted the repair of TH neurons in the substantia nigra region of mice, thus alleviating the symptoms of PD mice (Fig. 6h). Overall, SAFE nanoparticles smartly released siKeap1 in

the high-level ROS environment of PD diseased neurons, degraded Keap1 mRNA, and thus downregulated Keap1 expression. The downregulation of Keap1 inhibited the ubiquitination of Nrf2, which upregulated Nrf2. The upregulation of Nrf2 then activated ARE, thereby protecting mitochondria and repairing neurons by downregulating ROS, eventually contributing to SAFE nucleic acid therapy for PD (Fig. 6i).

### 3.6. Evaluation of the effect of CLI treatment

PD is an aging-related chronic disease. The long-term medication increases the risk of organ injuries, such as CLI, in PD patients. ROS is also a primary therapeutic target to alleviate CLI. CCL<sub>4</sub> was injected intraperitoneally to construct CLI mouse models. The SAFE nanoparticles were injected intravenously twice a week for 12 times in CLI mice (Fig. 7a). CCL<sub>4</sub> significantly increased the activity of AST and ALT in blood, indicating that CCL<sub>4</sub> seriously impaired liver function. AST and ALT were significantly reduced in CLI mice after SAFE treatment, and there was no significant difference between the treatment effects of these three kinds of SAFE nanoparticles (Fig. 7b and c). In addition, the liver index of CLI mice was significantly reduced after SAFE nanoparticles treatment (Fig. S31). These results indicated that all these SAFE nanoparticles had excellent CLI treatment effects.

These SAFE nanoparticles also enhanced Nrf2 in the liver by downregulating the expression of Keap1 (Figs. S32 and S33). The

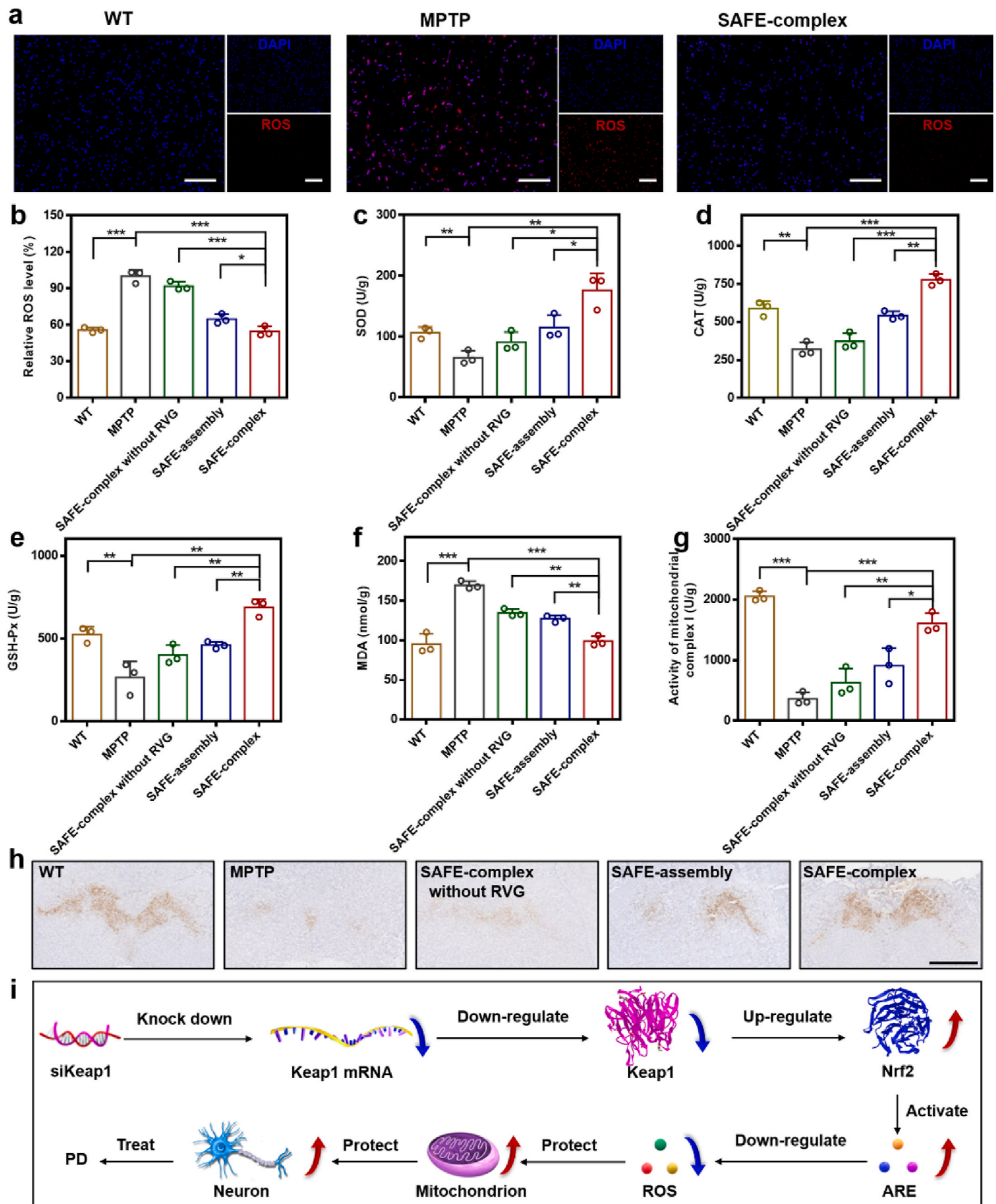
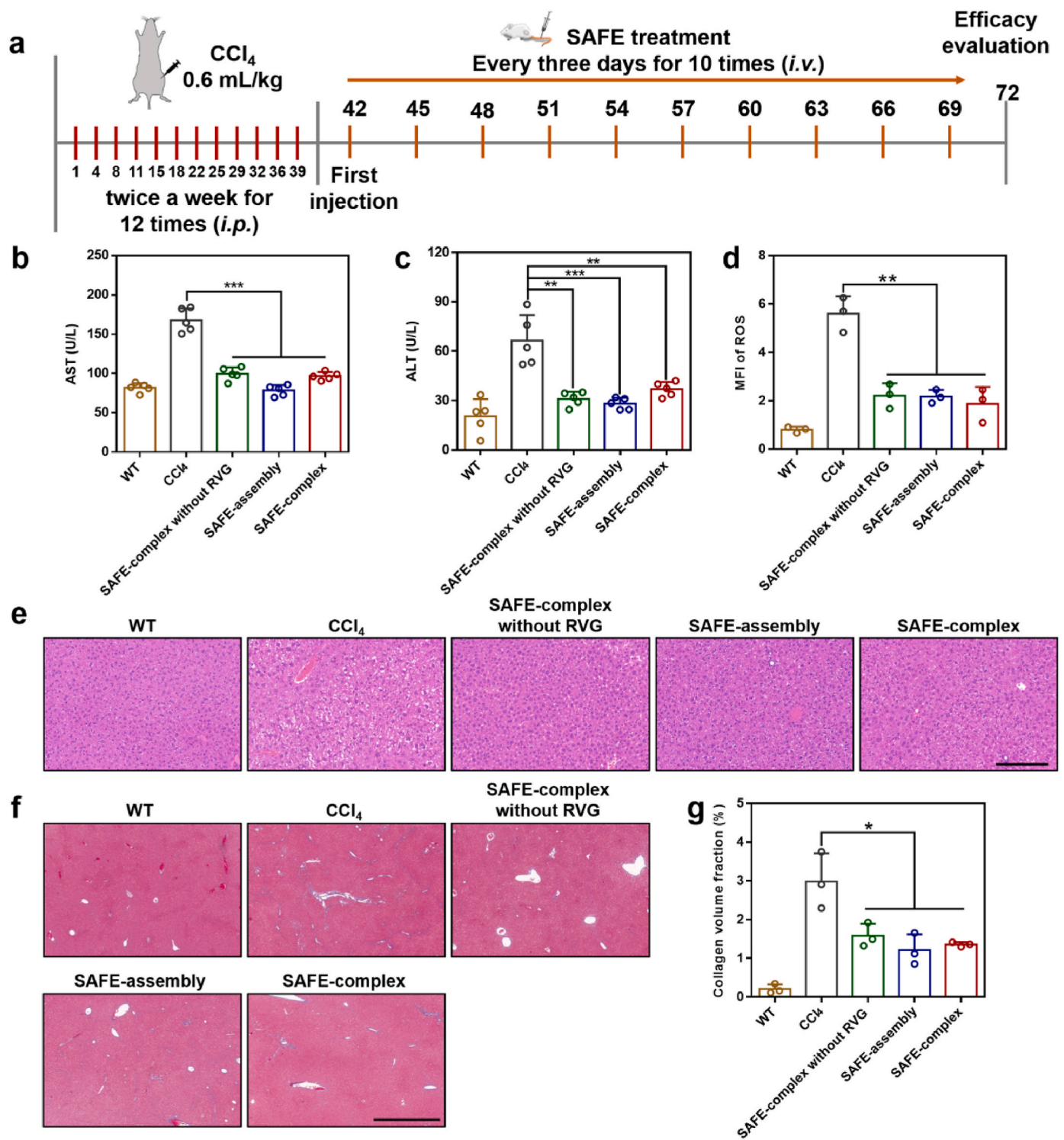


Fig. 6. *In vivo* therapeutic mechanisms of SAFE nanoparticles in PD. **a** The ROS level in the nigrostriatal region measured by immunofluorescence sections. Scale bar: 100  $\mu$ m **b** The ROS level in the brain measured by a ROS detection kit. **c–e** The antioxidant activity in the brain measured by ELISA. **f** The MDA content in the brain. **g** The activity of mitochondrial complex I in the brain measured by ELISA. **h** TH-staining immunohistochemistry sections in mice substantia nigra region. Scale bar: 1 mm. **i** Schematic diagram of the SAFE nucleic acid therapy mechanism for PD. Data were presented as the mean  $\pm$  SD ( $n = 3$ ). (*t*-test, \* $p < 0.05$ , \*\* $p < 0.01$ , \*\*\* $p < 0.001$ ).



**Fig. 7.** *In vivo* therapeutic effects and mechanisms of SAFE nanoparticles in CLI. **a** The construction and therapeutic schedule of CLI model mice. **b** The activity of AST measured by a Mindray BS-420 automatic biochemical analyzer. Data were presented as the mean  $\pm$  SD ( $n = 5$ ). **c** The activity of ALT measured by a Mindray BS-420 automatic biochemical analyzer. Data were presented as the mean  $\pm$  SD ( $n = 5$ ). **d** The quantitative results of ROS level in Fig. S34. Data were presented as the mean  $\pm$  SD ( $n = 3$ ). **e** H&E immunohistochemical sections in the livers. Scale bar: 200  $\mu$ m. **f** Masson immunohistochemical sections in the livers. Scale bar: 1 mm **g** The collagen volume fraction in the livers quantified from Fig. 7f. Data were presented as the mean  $\pm$  SD ( $n = 3$ ). (t-test, \*\* $p < 0.01$ , \*\*\* $p < 0.001$ ).

enhancement of Nrf2 activated the endogenous antioxidant system to scavenge excess ROS in the liver of CLI mice, thus protecting hepatocytes from oxidative stress (Figs. S24 and 7d). The large number of vacuoles in H&E sections of CLI mice's livers indicated that CCl<sub>4</sub> caused severe liver lesions. SAFE nucleic acid therapy significantly improved CLI (Fig. 7e). Masson sections of CLI mice exhibited slight fibrosis in the

liver. The SAFE-complex without RVG, the SAFE-assembly, and the SAFE-complex slightly alleviated fibrosis in CLI mice (Fig. 7f and g). These results showed the promise of SAFE nucleic acid therapy to enhancing the safety of neurodegenerative disease treatment by improving organ injuries.

#### 4. Conclusions

We proposed SAFE nucleic acid therapy to safely treat ROS-related chronic diseases and their comorbidities by smartly recovering the redox homeostasis of diseased cells through ROS-responsive nucleic acid drug release. In the case of PD&CLI, we one-step controllably synthesized the SAFE-complex based on nano-hybrid complexes to validate the potential of SAFE nucleic acid therapy. Compared to the SAFE-assembly, the SAFE-complex had superior freeze-drying stability and serum stability, thus enabling stable storage as a freeze-dried powder dosage form and facilitating *in vivo* delivery. The homogeneous monodisperse structure and RVG modification facilitated the accumulation of the SAFE-complex in brain neurons. Smartly released siKeap1 in the high-level ROS environment of diseased neurons restored redox homeostasis by activating the Keap1-Nrf2-ARE endogenous antioxidant pathway in an exogenous antioxidant-independent manner, reducing the safety risk of antioxidant treatment. In addition, SAFE nanoparticles metabolized to the liver alleviated CLI through the SAFE strategy, contributing to the safety of long-term dosing in PD patients. This SAFE nucleic acid therapy provided new avenues for safely treating ROS-related chronic diseases and their comorbidities.

#### CRedit authorship contribution statement

**Zhiguo Lu:** Conceptualization, Methodology, Investigation, Writing – original draft. **Ruichen Zhao:** Methodology, Investigation, Data curation, Writing – review & editing. **Yi Li:** Data curation, Investigation. **Jianze Wang:** Data curation. **Jing Guo:** Validation. **Chaobo Bai:** Data curation. **Jing Chen:** Investigation. **Jun Yang:** Validation. **Yiwan Geng:** Investigation. **Tianlu Zhang:** Validation. **Yanyue Wu:** Writing – review & editing. **Xiyue Jiao:** Validation. **Yining Wang:** Resources, Supervision. **Junliang Yuan:** Resources, Supervision. **Xin Zhang:** Resources, Writing – review & editing, Supervision, Project administration, Funding acquisition.

#### Declaration of competing interest

The authors declare that they have no known competing financial interests or personal relationships that could have appeared to influence the work reported in this paper. And Zhang Xin is an editorial board member for Bioactive Materials and was not involved in the editorial review or the decision to publish this article. All authors declare that there are no competing interests.

All animal experiments in this article were performed in accordance with guidelines evaluated and approved by the Institutional Animal Care and Use Committee (IACUC-AMSS-20230321-01).

#### Acknowledgments

Zhiguo Lu, Ruichen Zhao and Yi Li have contributed equally to this work. This work was supported by the National Natural Science Foundation of China (Nos. 32225029, 22205240, 52073287, 22075289, and 82071552).

#### Appendix A. Supplementary data

Supplementary data to this article can be found online at <https://doi.org/10.1016/j.bioactmat.2023.09.004>.

#### References

- [1] A. Sirelkhatim, S. Mahmud, A. Seeni, N.H.M. Kaus, L.C. Ann, et al., Review on zinc oxide nanoparticles: antibacterial activity and toxicity mechanism, *Nano-Micro Lett.* 7 (2015) 219–242, <https://doi.org/10.1007/s40820-015-0040-x>.
- [2] G. Filomeni, D. De Zio, F. Ceconci, Oxidative stress and autophagy: the clash between damage and metabolic needs, *Cell Death Differ.* 22 (2015) 377–388, <https://doi.org/10.1038/cdd.2014.150>.
- [3] B. Ezraty, A. Gennaris, F. Barras, J.F. Collet, Oxidative stress, protein damage and repair in bacteria, *Nat. Rev. Microbiol.* 15 (2017) 385–396, <https://doi.org/10.1038/nrmicro.2017.26>.
- [4] D.A. Butterfield, B. Halliwell, Oxidative stress, dysfunctional glucose metabolism and Alzheimer disease, *Nat. Rev. Neurosci.* 20 (2019) 148–160, <https://doi.org/10.1038/s41583-019-0132-6>.
- [5] J.G. Yan, P. Zhang, J. Tan, M. Li, X.F. Xu, et al., Cdk5 phosphorylation-induced SIRT2 nuclear translocation promotes the death of dopaminergic neurons in Parkinson's disease, *Npj Parkinsons Dis* 8 (2022) 135, <https://doi.org/10.1038/s41531-022-00311-0>.
- [6] B.B. Ratliff, W. Abdulmahdi, R. Pawar, M.S. Wolin, Oxidant mechanisms in renal injury and disease, *Antioxidants Redox Signal.* 25 (2016) 119–146, <https://doi.org/10.1089/ars.2016.6665>.
- [7] Y.X. Zhang, P. Murugesan, K. Huang, H. Cai, NADPH oxidases and oxidase cROSstalk in cardiovascular diseases: novel therapeutic targets, *Nat. Rev. Cardiol.* 17 (2020) 170–194, <https://doi.org/10.1038/s41569-019-0260-8>.
- [8] K. Du, A. Ramachandran, H. Jaeschke, Oxidative stress during acetaminophen hepatotoxicity: sources, pathophysiological role and therapeutic potential, *Redox Biol.* 10 (2016) 148–156, <https://doi.org/10.1016/j.redox.2016.10.001>.
- [9] P. Yang, T.Y. Wang, J.H. Zhang, H.J. Zhang, W.J. Bai, et al., Manipulating the antioxidative capacity of melanin-like nanoparticles by involving condensation polymerization, *Sci. China Chem.* 66 (2023) 1520–1528, <https://doi.org/10.1007/s11426-023-1542-8>.
- [10] M.C. Lu, J.A. Ji, Z.Y. Jiang, Q.D. You, The Keap1-Nrf2-ARE pathway as a potential preventive and therapeutic target: an update, *Med. Res. Rev.* 36 (2016) 924–963, <https://doi.org/10.1002/med.21396>.
- [11] W.J. Tu, H. Wang, S. Li, Q. Liu, H. Sha, The anti-inflammatory and anti-oxidant mechanisms of the Keap1/Nrf2/ARE signaling pathway in chronic diseases, *Aging Dis* 10 (2019) 637–651, <https://doi.org/10.14336/Ad.2018.0513>.
- [12] J.D. Hayes, A.T. Dinkova-Kostova, The Nrf2 regulatory network provides an interface between redox and intermediary metabolism, *Trends Biochem. Sci.* 39 (2014) 199–218, <https://doi.org/10.1016/j.tibs.2014.02.002>.
- [13] X.Z. Dai, X.Q. Yan, K.A. Wintergerst, L. Cai, B.B. Keller, et al., Nrf2: redox and metabolic regulator of stem cell state and function, *Trends Mol. Med.* 26 (2020) 185–200, <https://doi.org/10.1016/j.molmed.2019.09.007>.
- [14] H. Sies, D.P. Jones, Reactive oxygen species (ROS) as pleiotropic physiological signalling agents, *Nat. Rev. Mol. Cell Biol.* 21 (2020) 363–383, <https://doi.org/10.1038/s41580-020-0230-3>.
- [15] A. Cuadrado, A.I. Rojo, G. Wells, J.D. Hayes, S.P. Cousins, et al., Therapeutic targeting of the NRF2 and KEAP1 partnership in chronic diseases, *Nat. Rev. Drug Discov.* 18 (2019) 295–317, <https://doi.org/10.1038/s41573-018-0008-x>.
- [16] H. Sies, V.V. Belousov, N.S. Chandel, M.J. Davies, D.P. Jones, et al., Defining roles of specific reactive oxygen species (ROS) in cell biology and physiology, *Nat. Rev. Mol. Cell Biol.* 23 (2022) 499–515, <https://doi.org/10.1038/s41580-022-00456-z>.
- [17] M.P. Murphy, H. Bayir, V. Belousov, C.J. Chang, K.J.A. Davies, et al., Guidelines for measuring reactive oxygen species and oxidative damage in cells and *in vivo*, *Nat. Metab.* 4 (2022) 651–662, <https://doi.org/10.1038/s42255-022-00591-z>.
- [18] H. Zhang, C. Huang, J. Zhang, C. Wang, T. Wang, et al., Synthetic fungal melanin nanoparticles with excellent antioxidative property, *Giant* 12 (2022), 100120, <https://doi.org/10.1016/j.giant.2022.100120>.
- [19] P. Yang, Z. Gu, F. Zhu, Y. Li, Structural and functional tailoring of melanin-like polydopamine radical scavengers, *CCS Chem.* 2 (2020) 128–138, <https://doi.org/10.31635/ccschem.020.201900077>.
- [20] B. Hu, L.P. Zhong, Y.H. Weng, L. Peng, Y.Y. Huang, et al., Therapeutic siRNA: state of the art, *Signal Transduct. Targeted Ther.* 5 (2020) 101, <https://doi.org/10.1038/s41392-020-0207-x>.
- [21] Z.G. Lu, J. Shen, J. Yang, J.W. Wang, R.C. Zhao, et al., Nucleic acid drug vectors for diagnosis and treatment of brain diseases, *Signal Transduct. Targeted Ther.* 8 (2023) 39, <https://doi.org/10.1038/s41392-022-01298-z>.
- [22] X. Liu, J.J. Xiang, D.C. Zhu, L.M. Jiang, Z.X. Zhou, et al., Fusogenic reactive oxygen species triggered charge-reversal vector for effective gene delivery, *Adv. Mater.* 28 (2016) 1743–1752, <https://doi.org/10.1002/adma.201504288>.
- [23] W.H. Ji, Y. Li, R.Y. Liu, Z.G. Lu, L.Y. Liu, et al., Synaptic vesicle-inspired nanoparticles with spatiotemporally controlled release ability as a "nanoguard" for synergistic treatment of synucleinopathies, *Mater. Horiz.* 8 (2021) 1199–1206, <https://doi.org/10.1039/d0mh01542c>.
- [24] Y. Han, C.H. Gao, H. Wang, J.J. Sun, M. Liang, et al., Macrophage membrane-coated nanocarriers co-modified by RVG29 and TPP improve brain neuronal mitochondria-targeting and therapeutic efficacy in Alzheimer's disease mice, *Bioact. Mater.* 6 (2021) 529–542, <https://doi.org/10.1016/j.bioactmat.2020.08.017>.
- [25] D.H. Huang, Q.W. Wang, Y.H. Cao, H.C. Yang, M. Li, et al., Multiscale NIR-II imaging-guided brain-targeted drug delivery using engineered cell membrane nanofunction for Alzheimer's disease therapy, *ACS Nano* 17 (2023) 5033–5046, <https://doi.org/10.1021/acsnano.2c12840>.
- [26] G.C. Terstappen, A.H. Meyer, R.D. Bell, W.D. Zhang, Strategies for delivering therapeutics across the blood-brain barrier, *Nat. Rev. Drug Discov.* 20 (2021) 362–383, <https://doi.org/10.1038/s41573-021-00139-y>.
- [27] K. Ulbrich, K. Hala, V. Subr, A. Bakandritsos, J. Tucek, et al., Targeted drug delivery with polymers and magnetic nanoparticles: covalent and noncovalent approaches, release control, and clinical studies, *Chem. Rev.* 116 (2016) 5338–5431, <https://doi.org/10.1021/acs.chemrev.5b00589>.
- [28] J. Shen, Z.G. Lu, J.Z. Wang, Q.L. Hao, W.H. Ji, et al., Traceable nano-biohybrid complexes by one-step synthesis as CRISPR-chem vectors for neurodegenerative diseases synergistic treatment, *Adv. Mater.* 33 (2021), 2101993, <https://doi.org/10.1002/adma.202101993>.

- [29] N. Yin, Y.Z. Zhao, C.H. Liu, Y. Yang, Z.H. Wang, et al., Engineered nanoerythrocytes alleviate central nervous system inflammation by regulating the polarization of inflammatory microglia, *Adv. Mater.* 34 (2022), 2201322, <https://doi.org/10.1002/adma.202201322>.
- [30] J.M. Metzger, Y.Y. Wang, S.S. Neuman, K.J. Snow, S.A. Murray, et al., Efficient in vivo neuronal genome editing in the mouse brain using nanocapsules containing CRISPR-Cas9 ribonucleoproteins, *Biomaterials* 293 (2023), 121959, <https://doi.org/10.1016/j.biomaterials.2022.121959>.
- [31] Z.G. Lu, Y. Li, Y.J. Shi, Y.H. Li, Z.B. Xiao, et al., Traceable nanoparticles with spatiotemporally controlled release ability for synergistic glioblastoma multiforme treatment, *Adv. Funct. Mater.* 27 (2017), 1703967, <https://doi.org/10.1002/adfm.201703967>.
- [32] J. Yoo, E. Lee, H.Y. Kim, D.H. Youn, J. Jung, et al., Electromagnetized gold nanoparticles mediate direct lineage reprogramming into induced dopamine neurons in vivo for Parkinson's disease therapy, *Nat. Nanotechnol.* 12 (2017) 1006–1014, <https://doi.org/10.1038/Nnano.2017.133>.
- [33] L.Y. Liu, Y. Li, H. Peng, R.Y. Liu, W.H. Ji, et al., Targeted exosome coating gene-chem nanocomplex as "nanoscavenger" for clearing  $\alpha$ -synuclein and immune activation of Parkinson's disease, *Sci. Adv.* 6 (2020), eaba3967, <https://doi.org/10.1126/sciadv.aba3967>.
- [34] Z.G. Lu, J.Z. Wang, L.N. Qu, G.H. Kan, T.L. Zhang, et al., Reactive mesoporous silica nanoparticles loaded with limonene for improving physical and mental health of mice at simulated microgravity condition, *Bioact. Mater.* 5 (2020) 1127–1137, <https://doi.org/10.1016/j.bioactmat.2020.07.006>.
- [35] C. Baeck, A. Wehr, K.R. Karlmark, F. Heymann, M. Vucur, et al., Pharmacological inhibition of the chemokine CCL2 (MCP-1) diminishes liver macrophage infiltration and steatohepatitis in chronic hepatic injury, *Gut* 61 (2012) 416–426, <https://doi.org/10.1136/gutjnl-2011-300304>.
- [36] T. Van de Vyver, S.C. De Smedt, K. Raemdonck, Modulating intracellular pathways to improve non-viral delivery of RNA therapeutics, *Adv. Drug Deliv. Rev.* 181 (2022), 114041, <https://doi.org/10.1016/j.addr.2021.114041>.
- [37] C.H. Albertsen, J.A. Kulkarni, D. Witzigmann, M. Lind, K. Petersson, et al., The role of lipid components in lipid nanoparticles for vaccines and gene therapy, *Adv. Drug Deliv. Rev.* 188 (2022), 114416, <https://doi.org/10.1016/j.addr.2022.114416>.
- [38] D.J. Hare, P.A. Adlard, P.A. Doble, D.I. Finkelstein, Metallobiology of 1-methyl-4-phenyl-1,2,3,6-tetrahydropyridine neurotoxicity, *Metalomics* 5 (2013) 91–109, <https://doi.org/10.1039/c2mt20164j>.
- [39] M.L. Zhao, J.L. Chen, K.M. Mao, H. She, Y.X. Ren, et al., Mitochondrial calcium dysfunction contributes to autophagic cell death induced by MPP+ via AMPK pathway, *Biochem. Biophys. Res. Commun.* 509 (2019) 390–394, <https://doi.org/10.1016/j.bbrc.2018.12.148>.
- [40] J. Zielonka, J. Joseph, A. Sikora, M. Hardy, O. Ouari, et al., Mitochondria-targeted triphenylphosphonium-based compounds: syntheses, mechanisms of action, and therapeutic and diagnostic applications, *Chem. Rev.* 117 (2017) 10043–10120, <https://doi.org/10.1021/acs.chemrev.7b00042>.
- [41] J.A. Amorim, G. Coppotelli, A.P. Rolo, C.M. Palmeira, J.M. Ross, et al., Mitochondrial and metabolic dysfunction in ageing and age-related diseases, *Nat. Rev. Endocrinol.* 18 (2022) 243–258, <https://doi.org/10.1038/s41574-021-00626-7>.
- [42] T. Kikuchi, A. Morizane, D. Doi, H. Magotani, H. Onoe, et al., Human iPSC cell-derived dopaminergic neurons function in a primate Parkinson's disease model, *Nature* 548 (2017) 592–596, <https://doi.org/10.1038/nature23664>.
- [43] B. Rosin, M. Slovik, R. Mitelman, M. Rivlin-Etzion, S.N. Haber, et al., Closed-loop deep brain stimulation is superior in ameliorating Parkinsonism, *Neuron* 72 (2011) 370–384, <https://doi.org/10.1016/j.neuron.2011.08.023>.
- [44] Z.Q. Li, X.Q. Chang, M.H. Hu, J.K.H. Fang, I.M. Sokolova, et al., Is microplastic an oxidative stressor? Evidence from a meta-analysis on bivalves, *J. Hazard Mater.* 423 (2022), 127211, <https://doi.org/10.1016/j.jhazmat.2021.127211>.
- [45] K. Naraki, R. Rezaee, G. Karimi, A review on the protective effects of naringenin against natural and chemical toxic agents, *Phytother. Res.* 35 (2021) 4075–4091, <https://doi.org/10.1002/ptr.7071>.
- [46] N.T. Moldogazieva, I.M. Mokhosoev, T.I. Mel'nikova, Y.B. Porozov, A.A. Terentiev, Oxidative stress and advanced lipoxidation and glycation end products (ALEs and AGEs) in aging and age-related diseases, *Oxid. Med. Cell. Longev.* (2019), 3085756, <https://doi.org/10.1155/2019/3085756>, 2019.
- [47] G. Barrera, S. Pizzimenti, M. Daga, C. Dianzani, A. Arcaro, et al., Lipid peroxidation-derived aldehydes, 4-hydroxynonenal and malondialdehyde in aging-related disorders, *Antioxidants-Basel* 7 (2018) 102, <https://doi.org/10.3390/antiox7080102>.